

Low Energy Carbon Capture via Electrochemically Induced pH Swing with Electrochemical Rebalancing

Shijian Jin[†], Min Wu[†], Yan Jing[‡], Roy G. Gordon[‡] and Michael J. Aziz^{†*}

[†] John A. Paulson School of Engineering and Applied Sciences, Harvard University, Cambridge, Massachusetts, 02138, United States

[‡]Department of Chemistry and Chemical Biology, Harvard University, Cambridge, Massachusetts 02138, United States

*maziz [at] harvard [dot] edu

Abstract

We demonstrate a carbon capture system based on pH swing cycles driven through proton-coupled electron transfer of sodium (3,3'-(phenazine-2,3-diylbis(oxy))bis(propene-1-sulfonate)) (DSPZ) molecules. Electrochemical reduction of DSPZ causes an increase of hydroxide concentration, which absorbs CO₂; subsequent electrochemical oxidation of the reduced DSPZ consumes the hydroxide, causing CO₂ outgassing. The measured electrical work of separating CO₂ from a binary mixture with N₂, at CO₂ inlet partial pressures ranging from 0.1 to 0.5 bar, and releasing to a pure CO₂ exit stream at 1.0 bar, was measured for electrical current densities of 20 to 150 mA cm⁻². The work for separating CO₂ from a 0.1 bar inlet and concentrating into 1 bar exit is 61.3 kJ mol_{CO₂}⁻¹ at a current density of 20 mA cm⁻² and extrapolates to 57.1 kJ mol_{CO₂}⁻¹ in the low-current-density limit. At this limit, the cycle work for capture from 0.4 mbar extrapolates to 108–212 kJ mol_{CO₂}⁻¹ depending on the initial composition of the electrolyte. We also introduce an electrochemical rebalancing method that extends cell lifetime by recovering the initial electrolyte composition after it is perturbed by side reactions. We discuss the implications of these results for future low-energy electrochemical carbon capture devices.

Introduction

Accumulating CO₂ emissions from anthropogenic activities constitute the major cause of global climate change.^{1, 2} While efforts are being made in switching from fossil fuel-based energy to virtually emissions-free sources such as nuclear, solar, wind and geothermal, fossil fuel combustion will remain an important component of the world economy for a long time.³ Consequently, carbon removal — whether captured from a point source^{2, 4-8} such as a combustion power plant or directly from the air (a.k.a. direct air capture, DAC) or the ocean^{2, 9-13} — in order to reduce atmospheric CO₂ concentrations, is gaining increasing attention.

Numerous methods for point source capture and DAC have been developed. Among the most studied is wet amine scrubbing for point source capture⁴⁻⁶ and strongly alkaline (pH > 14) solution for DAC,^{2, 9} both of which rely on a large temperature-swing cycle to regenerate sorbents. Although sorbent composition has been optimized to lower the energy cost for both strategies, the thermal energy requirement for heating is still ~100 kJ mol_{CO₂}⁻¹ for point source capture^{6, 14, 15}

and $>150 \text{ kJ mol}_{\text{CO}_2}^{-1}$ for DAC.^{10, 16} In addition, sorbent volatility, toxicity and corrosivity cause environmental concerns.² Methods that remove CO_2 from the ocean, which allow it to absorb more CO_2 , have also been studied, but the high water-handling requirement is a challenge.^{12, 13}

Electrochemically mediated separation technologies constitute an increasingly attractive alternative to traditional temperature-swing or pressure-swing methods because of the rapidly decreasing cost of intermittent renewable electricity and the mild operating conditions of ambient temperature and pressure.^{7, 8, 13, 17-20} However, most existing methods operate at low current density ($< 5 \text{ mA cm}^{-2}$) because of large overpotentials and the corresponding energetic cost at higher current density, implying a high capital cost of electrochemical hardware. Recently, our group proposed and demonstrated a pH swing cycle for CO_2 separation electrochemically driven through proton-coupled electron transfer (PCET) of redox active organic molecules (“Q”).¹⁸ In this scheme, proton-coupled electrochemical reduction of these molecules ($\text{Q} + 2\text{H}_2\text{O} + 2\text{e}^- \rightarrow \text{QH}_2 + 2\text{OH}^-$) raises the electrolyte pH and total alkalinity (TA), leading to CO_2 capture from point source or air and conversion to dissolved inorganic carbon (DIC); subsequent electrochemical oxidation of the reduced molecules ($\text{QH}_2 + 2\text{OH}^- \rightarrow \text{Q} + 2\text{H}_2\text{O} + 2\text{e}^-$) acidifies the electrolyte and lowers TA, resulting in the conversion of DIC to CO_2 gas and its release.

Here, we report a proof-of-concept point source (10 %) CO_2 separation system that uses a sodium (3,3’-(phenazine-2,3-diylbis(oxy))bis(propane-1-sulfonate)), i.e. DSPZ, based electrochemical pH-swing cell with an energy cost of only $61.3 \text{ kJ mol}_{\text{CO}_2}^{-1}$ at 20 mA cm^{-2} . Through analyzing the cycle work obtained under systematically varied inlet partial pressure and current density, we estimate that the cost for capturing from a 0.4 mbar CO_2 inlet using this system extrapolates to $108\text{--}212 \text{ kJ mol}_{\text{CO}_2}^{-1}$ in the low-current-density limit, and that it can be further lowered if a higher concentration of DSPZ, or other PCET-active molecules, is used. Recognizing the sensitivity of the reduced form of DSPZ, i.e. DSPZH₂, to chemical oxidation by atmospheric or dissolved O_2 , we introduce and demonstrate an electrochemical rebalancing method that expels oxygen from solution and restores the initial composition of the electrolytes.

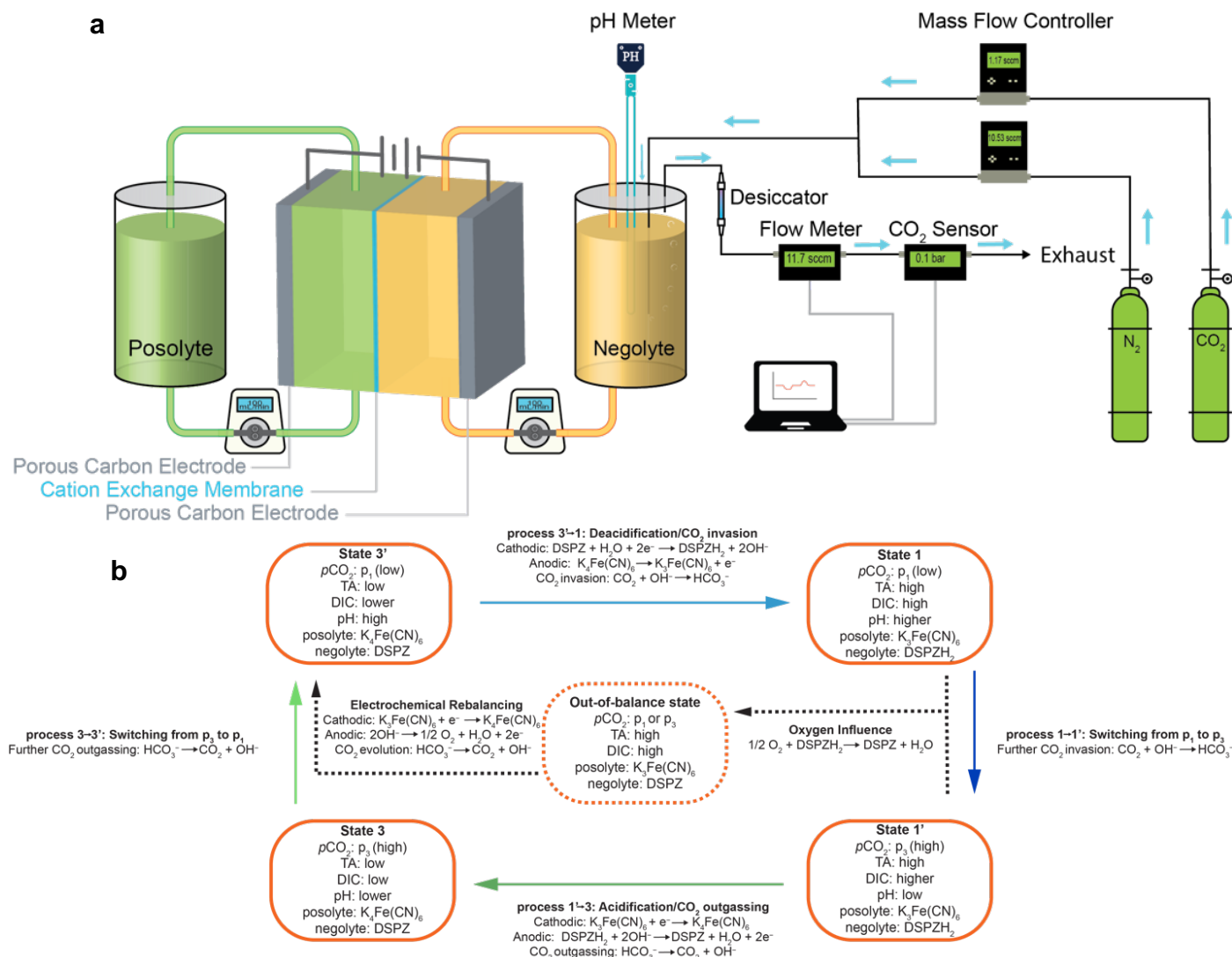


Fig. 1| Scheme of the pH swing carbon capture flow system. a, Schematic of the Fe(CN)₆ (posolyte) | DSPZ (negolyte) flow cell and full system. Blue arrows indicate gas flow direction. Adapted from Jin *et al.*¹⁸ **b**, Process flow. The solid arrows refer to desired reactions in a complete carbon capture/release cycle. The carbonate formation and decomposition reactions are neglected for simplicity. The dashed arrow on the right side refers to the side reaction caused by oxygen and the dashed arrow on the left refers to reactions in the electrochemical rebalancing step.

Device Setup and Process Flow

Fig. 1a shows the schematic of the Fe(CN)₆ | DSPZ carbon capture flow cell and the hardware for providing the gas mixture and analyzing the exhaust. The upstream gas composition in the negolyte headspace was controlled by CO₂ and N₂ mass flow controllers (MFCs). Downstream of the desiccator, the total gas flow rate and CO₂ partial pressure were measured using a digital flow meter and a CO₂ sensor, respectively. A pH probe immersed in the negolyte solution reported the temporal evolution of its pH, which enabled the tracking of TA and DIC in real time.¹⁸ **Fig. 1b** illustrates the electrolyte composition in the four states of the pH swing carbon capture cycle and the processes connecting the states. We denote the CO₂ partial pressure during the CO₂ capture process as the inlet pressure or p_1 , and that during the CO₂ outgassing process as the exit pressure

or p_3 . Similarly, the subscripts following TA or DIC refer to the TA and DIC of the corresponding states. The naming convention for the states is adopted from previous work,¹⁸ where the equilibrium and constraints governing pH, TA, DIC and $p\text{CO}_2$ are explained in detail. The four sequential processes are $3'_{\text{i}} \rightarrow 1$: two-stage deacidification+ CO_2 invasion (inlet); $1 \rightarrow 1'$: change of the headspace atmosphere from inlet to exit pressure, i.e. switching from p_1 to p_3 ; $1' \rightarrow 3$: two-stage acidification+ CO_2 outgassing (exit) and $3 \rightarrow 3'_{\text{f}}$: change of the headspace atmosphere from exit to inlet pressure, i.e. switching from p_3 to p_1 (**Fig. 1b**, four arrows). Note that, as DSPZH_2 is reversibly chemically oxidized by atmospheric O_2 to DSPZ, the posolyte supplies extra charge to electrochemically reduce the extra oxidized DSPZ; this is reflected in the low Coulombic efficiency of the cell and an accumulation of TA and DIC in the negolyte. This process also transforms more of the posolyte to its oxidized form, i.e. $[\text{K}^+]_4[\text{Fe}^{\text{II}}(\text{CN})_6]^{4-} \rightarrow [\text{K}^+]_3[\text{Fe}^{\text{III}}(\text{CN})_6]^{3-} + \text{e}^-$, than at a similar point in the previous deacidification-acidification cycle. During cell operation reduction on one side must be accompanied by oxidation on the other side but, as the available fraction of reduced species on the posolyte side, i.e. $[\text{K}^+]_4[\text{Fe}^{\text{II}}(\text{CN})_6]^{4-}$, decreases, the cell can access less and less of its theoretical capacity during its oxidation-reduction oscillations; this is reflected in the decaying capacity of the cell. Eventually both sides become 100% oxidized and cell operation ceases. Our remedy for such situation is the electrochemical rebalancing method explained later in the text.

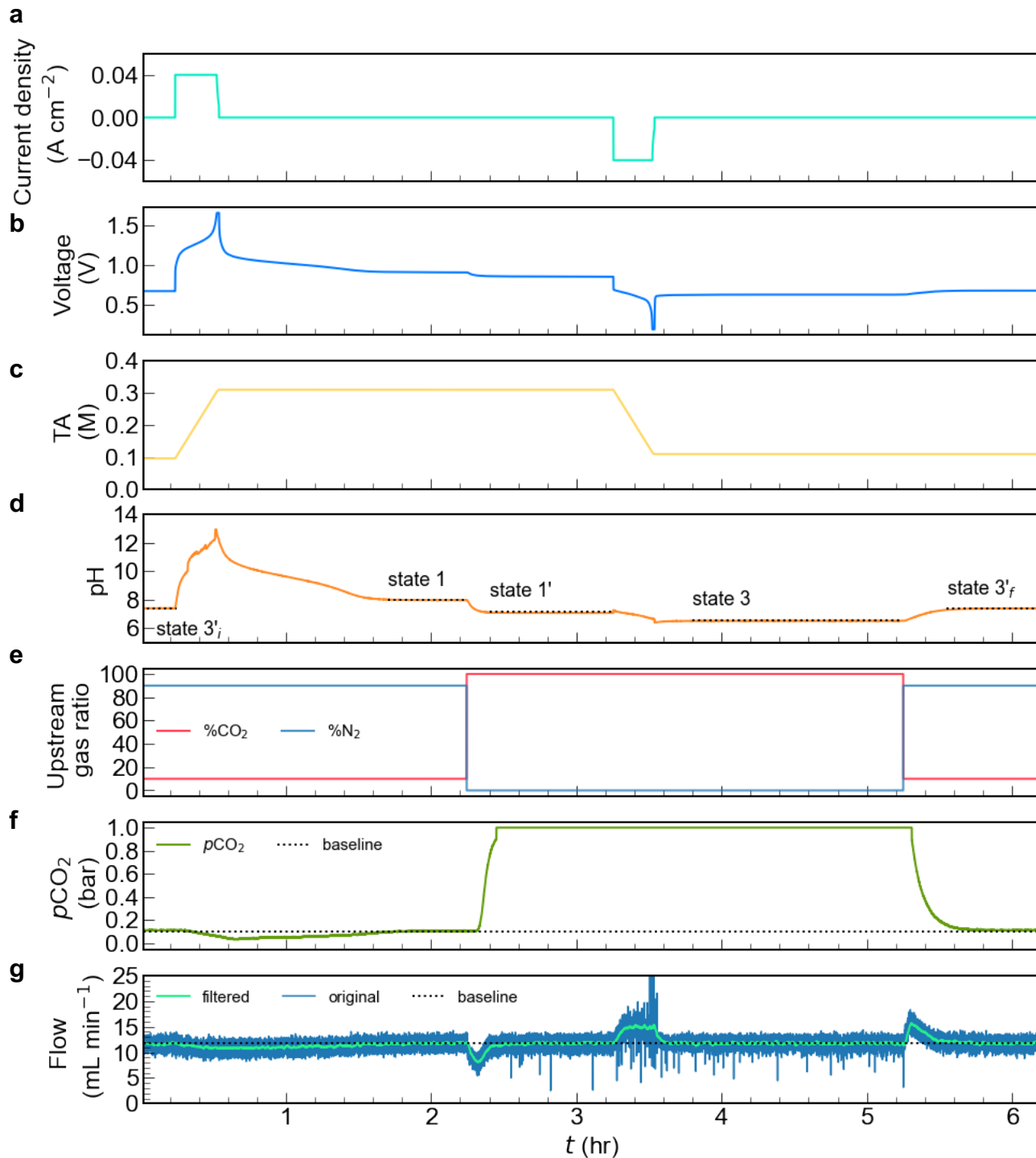


Fig. 2| A CO₂ concentrating cycle with inlet pressure $p_1 = 0.1$ bar and exit pressure $p_3 = 1$ bar using a DSPZ-based flow cell at 40 mA cm^{-2} . Electrolytes comprised 10 mL 0.11 M DSPZ in 1 M KCl (negolyte, capacity limiting) and 35 mL 0.1 M K₄Fe(CN)₆ and 0.04 M K₃Fe(CN)₆ in 1 M KCl (posolyte, non-capacity limiting). **a, Current density. **b**, Voltage. **c**, Total alkalinity. **d**, pH of the negolyte. States 3'_i, 1, 1', 3 and 3'_f represent pH values before deacidification under 0.1 bar $p\text{CO}_2$, after deacidification+absorption under 0.1 bar $p\text{CO}_2$, after changing $p\text{CO}_2$ from 0.1 bar to 1 bar, after acidification+desorption under 1 bar and after changing $p\text{CO}_2$ from 1 bar to 0.1 bar, respectively. The detailed composition of these states is elaborated in **Table 1**. **e** N₂ and CO₂ percentage in the upstream source gas, controlled by mass flow controllers. **f**, downstream CO₂ partial pressure. The baseline indicates $p\text{CO}_2 = 0.1$ bar. **g**, downstream total gas flow rate; the baseline is 11.8 mL min^{-1} .**

One Carbon Capture Cycle with $p_1 = 0.1$ bar and $p_3 = 1$ bar at 40 mA cm^{-2}

In previous work we demonstrated a series of non-concentrating cycles, in which both exit and inlet $p\text{CO}_2$ were 0.47 bar, utilizing a DSPZ-based flow cell at $40\text{--}150 \text{ mA cm}^{-2}$.¹⁸ In the present work we show the use of this setup for CO_2 separation from low partial pressure in a mixture with nitrogen and release into a pure CO_2 exit stream at 1.0 bar. **Fig. 2** demonstrates one such cycle with $p\text{CO}_2 = 1.0$ and 0.1 bar at the exit and inlet, respectively. Beginning at state $3'_i$, the upstream CO_2 partial pressure was set to 0.1 bar, which is close to its value in the flue gas from either coal or natural gas fired power plants.⁷ We define t as the time elapsed. As deacidification began (**Fig. 2 a** and **b**, $t = 0.2$ hr), the TA went up at a linear rate because only K^+ ions crossed the cation exchange membrane (CEM) when a constant 40 mA cm^{-2} current density was applied (**Fig. 2 c**).¹⁸ As a result of the PCET reactions during the reduction of DSPZ, the negolyte pH (**Fig. 2 d**) increased from near neutral to ~ 13.5 at the end of the deacidification process, indicated by the steep increase of voltage until reaching the preset voltage cutoff of 1.65 V (**Fig. 2 b**, $t = 0.6$ hr). CO_2 invasion began when deacidification began but continued beyond the end of deacidification: invasion lasted until $t = 1.8$ hr, as indicated by the $p\text{CO}_2$ signal returning to the 0.1 bar baseline, because of the limited reaction rate between dilute OH^- and CO_2 . The deviation in the gas flow rate (**Fig. 2 g**) from the baseline starting at $t = 0.2$ hr and returning at 1.8 hr also documents the complete capture process. As CO_2 reacted with hydroxide and water to form CO_3^{2-} and HCO_3^- , the pH (**Fig. 2 d**) dropped from ~ 13.5 at $t = 0.5$ hr to 8.1 at 1.8 hr and then plateaued, once again indicating the completion of the capture process. The absorbed volume of CO_2 is 47 mL (eq. 1 in Methods). Assuming $T = 293 \text{ K}$, $p = 1$ bar and ideal gas behavior, this absorption causes a change in DIC of 0.20 M (2.0 mmol CO_2 in 10 mL negolyte volume). We denote this change as $\Delta\text{DIC}_{\text{flow},3'_i \rightarrow 1}$, where the subscript “flow” indicates that the value is measured by the downstream flowmeter and CO_2 sensor and “ $3'_i \rightarrow 1$ ” indicates that this value corresponds to the change in process $3'_i \rightarrow 1$ (**Table 1**). The same naming convention is used for both ΔTA and ΔDIC throughout the rest of this text. Unlike the flowmeter and CO_2 sensor, which quantify ΔDIC , the pH probe, in addition to providing a measured value (pH_{meas}), provides a direct measurement of DIC, because given two values from TA, DIC, $p\text{CO}_2$ and pH, the others can be derived.^{18, 21} At state $3'_i$, the DIC (regardless of subscripts) and TA values are calculated using pH_{meas} and assumed gas-solution equilibrium, i.e. $\text{CO}_2(\text{aq}) = 0.035 \times p\text{CO}_2$, where 0.035 comes from Henry’s law constant of 35 mM bar^{-1} for CO_2 at room temperature. Because $\Delta\text{TA}_{3'_i \rightarrow 1}$ is known from **Fig. 2 c**, TA_1 can be evaluated, and so can the TA values at other states. One way of obtaining DIC in all states except $3'_i$ and of obtaining ΔDIC values between all states is to use the known TA and $\text{CO}_2(\text{aq})$, and we denote these values with subscript “TA-eq” (**Table 1**). This method is also used to construct the ideal cycles [**ESI, Fig. S1**]. Another way to calculate DIC is to use the TA and pH_{meas} without assuming gas-solution equilibrium. We denote DIC and ΔDIC calculated this way with subscript “TA-pH”. The ΔDIC between state $3'_i$ and 1, i.e. 0.20 M, determined by flow meter and CO_2 sensor, i.e. $\Delta\text{DIC}_{\text{flow},3'_i \rightarrow 1}$, is corroborated by $\Delta\text{DIC}_{\text{TA-pH},3'_i \rightarrow 1}$ and $\Delta\text{DIC}_{\text{TA-eq},3'_i \rightarrow 1}$ (**Table 1**).

Table 1| Summary of TA, $p\text{CO}_2$, pH, DIC and ΔDIC . TA is calculated by counting charges and assuming K^+ is the only ion passing through the CEM; $p\text{CO}_2$ is the CO_2 partial pressure at each state; pH_{meas} refers to the negolyte pH measured by the pH probe. All DIC and TA values at state $3'_i$ are calculated using the measured pH and assuming gas-solution equilibrium. In all other states, $\text{pH}_{\text{TA-eq}}$ and $\text{DIC}_{\text{TA-eq}}$ are calculated using TA and assuming gas-solution equilibrium. $\text{DIC}_{\text{TA-pH}}$ is calculated using TA and pH_{meas} ; $\Delta\text{DIC}_{\text{TA-pH}}$ and $\Delta\text{DIC}_{\text{TA-eq}}$ are the difference in $\text{DIC}_{\text{TA-pH}}$ and $\text{DIC}_{\text{TA-eq}}$ values, respectively, between two consecutive states; $\Delta\text{DIC}_{\text{flow}}$ is converted from the volume of CO_2 captured or released, measured by the downstream flow meter and CO_2 sensor and DIC_{flow} is calculated by adding $\Delta\text{DIC}_{\text{flow}}$ at the current state to DIC_{flow} at the state one row above. Because $\Delta\text{DIC}_{\text{flow}}$ is not measurable between states 1 and $1'$

and states 3 and 3', DIC_{flow} at states 1' and 3' is calculated by adding DIC_{flow} with ΔDIC_{TA-pH} values between the corresponding states.

State	TA (M)	p_1, pCO_2 (bar)	pH_{meas}	pH_{TA-eq}	DIC_{flow} (M)	DIC_{TA-pH} (M)	DIC_{TA-eq} (M)	ΔDIC_{flow} (M)	ΔDIC_{TA-pH} (M)	ΔDIC_{TA-eq} (M)
3' _i	0.11 ^a	0.1	7.4	7.4 ^a	0.11 ^a	0.11 ^a	0.11 ^a			
1	0.32	0.1	8.1	7.9	0.31	0.31	0.31	0.20	0.20	0.20
1'	0.32	1.0	7.1	6.9	0.34 ^b	0.34	0.34	N/A	0.03	0.03
3	0.12	1.0	6.6	6.5	0.14	0.14	0.14	0.20	-0.20	-0.20
3' _f	0.12	0.1	7.5	7.5	0.12 ^c	0.12	0.12	N/A	-0.03	-0.03

^a All values derived from pH_{meas} , assuming gas-solution equilibrium
^b Calculated by summing $DIC_{flow,1}$ and $\Delta DIC_{TA-pH,1-1'}$
^c Calculated by summing $DIC_{flow,3}$ and $\Delta DIC_{TA-pH,3-3'}$

After CO₂ capture at 0.1 bar (p_1) was completed, the headspace of the negolyte was switched to a pure CO₂ environment (p_3) to prepare for CO₂ outgassing, i.e. going through process 1→1' (Fig. 2 e, $t = 2.2$ hr). The drop in flow rate at $t = 2.2$ hr and its return to the baseline at 2.5 hr is caused by the combined effect of mismatched valve response rate in the MFCs (the N₂ MFC valve closes faster than the CO₂ MFC valve opens) and a small increase in DIC due to increased pCO_2 in the headspace. This increase in DIC, corresponding to $\Delta DIC_{1 \rightarrow 1'}$, is difficult to quantify via the flowmeter and CO₂ sensor, but can be determined using pH_{meas} ($\Delta DIC_{TA-pH,1 \rightarrow 1'}$) or assuming gas-solution equilibrium ($\Delta DIC_{TA-eq,1 \rightarrow 1'}$), which both give 0.03 M (Table 1). The acidification+CO₂ outgassing (process 1'→3) started at $t = 3.2$ hr and ended at a little over 3.6 hr (Fig. 2 a-d and g). Note that, unlike in process 3'→1, the CO₂ outgassing, which is observable from pH change and an increase in flow rate, (Fig. 2 d and g) lasted for no more than ten minutes after the acidification process (Fig. 2 a and b) finished. The outgassed CO₂ volume was 49 mL (eq. 1), which is equivalent to $\Delta DIC_{flow,1' \rightarrow 3} = -0.20$ M. Once again, ΔDIC_{TA-pH} and ΔDIC_{TA-eq} agree with ΔDIC_{flow} for the changes between states 1' and 3. Starting from a little over $t = 5.2$ hr, the headspace was filled with 0.1 bar CO₂ + 0.9 bar N₂ to recover the state 3' for the next cycle (process 3→3'). Like process 1→1', there was a combined effect of valve response and additional CO₂ outgassing during process 3→3', causing an increase in flow rate (Fig. 2 g, $t = 5.2$ hr to 5.6 hr). Note that state 3'_f has slightly higher pH and 0.01 M more of TA and DIC than state 3'_i because of the influence of oxygen (Fig. 1 b).

Calculation of $\Delta DIC_{flow,3 \rightarrow 1}$ and Molar Cycle Work

The discussion above shows how $\Delta DIC_{flow,3' \rightarrow 1}$ and $\Delta DIC_{flow,1' \rightarrow 3}$ are obtained by gas flow measurement, but neither of these two quantities reflect the actual amount captured at 0.1 bar and released at 1.0 bar, because both states 3'_i and 1 are at $p_1 = 0.1$ bar while both states 1' and 3 are at $p_3 = 1$ bar. The important quantity is the difference in DIC between states 3 and 1. With help of TA and pH measurements, $\Delta DIC_{flow,1 \rightarrow 3}$ is evaluated as $\Delta DIC_{TA-pH,1 \rightarrow 1'} + \Delta DIC_{flow,1' \rightarrow 3} = -0.17$ M; equivalently, but with opposite sign, $\Delta DIC_{flow,3 \rightarrow 1} = \Delta DIC_{flow,3' \rightarrow 1} + \Delta DIC_{TA-pH,3 \rightarrow 3'f} = 0.17$ M, i.e., 1.7 mmol CO₂ in a 10 mL negolyte volume. Because sufficient gas-solution equilibrium is approached (Fig. 2 f and g), ΔDIC_{TA-eq} may also be used in place of ΔDIC_{TA-pH} in such calculations, resulting in the same values of $\Delta DIC_{flow,1 \rightarrow 3}$ and $\Delta DIC_{flow,3 \rightarrow 1}$.

In this cycle, the deacidification work into the system, $w_{\text{deacidification}}$, is 0.267 kJ and the acidification work, $w_{\text{acidification}}$, is -0.119 kJ (eq. 3). Dividing the cycle work, w_{cycle} (eq. 2), by 1.7 mmol CO_2 gives the molar cycle work of 87 kJ $\text{mol}_{\text{CO}_2}^{-1}$. This value is already competitive with commercial amine scrubbing processes,^{4, 6} and it can be further decreased by using membranes with lower ohmic resistance or molecules with lower electron transfer overpotential.²²

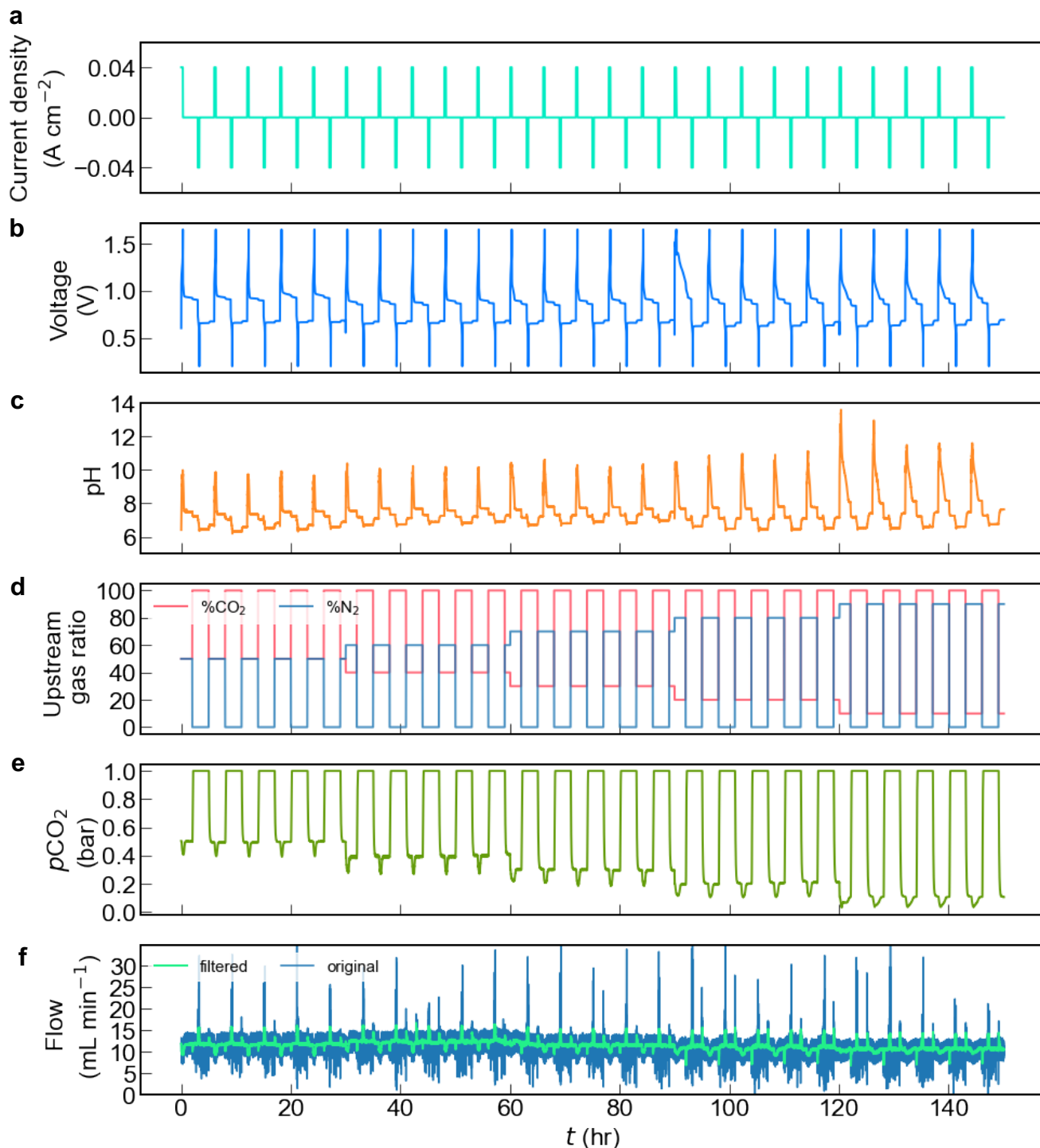


Fig. 3| Twenty five CO₂ concentrating cycles with 0.5, 0.4, 0.3, 0.2, and 0.1 bar inlet p_{CO_2} and 1 bar exit p_{CO_2} at 40 mA cm⁻². Same cell and negolyte as in Fig. 2 were employed. a, Current density. b, Voltage. c, pH of the negolyte. d, N₂ and CO₂ percentage in the upstream source gas, controlled by mass flow controllers; total pressure 1.0 bar. e, downstream CO₂ partial pressure. f, downstream total gas flow rate.

Carbon Capture Cycles with $p_1 = 0.1 - 0.5$ bar at 40 mA cm⁻²

In order to understand how the electrical work depends on the inlet p_{CO_2} , we performed five cycles each at $p_1 = 0.1$ to 0.5 bar with $p_3 = 1.0$ bar (**Fig. 3**). The same cell components and negolyte as in **Fig. 2** were used, and the posolyte was replaced with a fresh solution for each inlet condition to avoid oxygen-induced long-term cell imbalance (**Fig. 1b**).²³ **Fig S5b** shows that the CO₂ outgassing period is identical regardless of inlet p_{CO_2} because the exit p_{CO_2} is always 1 bar and the current density is always 40 mA cm⁻². In contrast, the capture period increases as inlet p_{CO_2} decreases (**ESI, Fig S5a**) because of the expected trend of reaction rate with decreasing reactant concentration. $\Delta\text{DIC}_{\text{flow},3 \rightarrow 1}$ values decrease as p_1 decreases (**Fig. 4a**) because of greater ΔDIC during processes $1 \rightarrow 1'$ and $3 \rightarrow 3'$ (vertical arrows in **Fig. 4c**) at smaller p_1 . The measured values closely align with the theoretical $\Delta\text{DIC}_{\text{TA-eq},3 \rightarrow 1}$ vs. p_1 curve (**Fig. 4a**).

This alignment permits us to estimate $\Delta\text{DIC}_{\text{flow},3 \rightarrow 1}$ for $p_1 = 0.4$ mbar and $p_3 = 1$ bar, i.e. similar to DAC conditions, by following the $\Delta\text{DIC}_{\text{TA-eq},3 \rightarrow 1}$ vs. p_1 curve to obtain a value of 0.049 M. Note that the $\Delta\text{DIC}_{\text{TA-eq},3 \rightarrow 1}$ vs. p_1 curve shifts downward as $\text{TA}_{3;i}$ increases (**ESI, Fig. S3b**). This has relatively small impacts on $\Delta\text{DIC}_{\text{TA-eq},3 \rightarrow 1}$ with high p_1 , but it causes significant differences for small p_1 values. For example, when $p_1 = 0.4$ mbar, $\Delta\text{DIC}_{\text{TA-eq},3 \rightarrow 1}$ for $\text{TA}_{3;i} = 0, 0.11$ and 0.21 M is 0.096, 0.049 and 0.005 M, respectively (**ESI, Fig. S1-3**). Because $\Delta\text{DIC}_{3 \rightarrow 1}$ is in the denominator when CO₂ molar cycle work is calculated, lowering $\Delta\text{DIC}_{3 \rightarrow 1}$ increases the molar energy cost accordingly (**ESI, Fig. S2b and c**). High $\text{TA}_{3;i}$ should therefore be avoided, and a necessary step to achieve this goal is to limit the impact of oxidation of DSPZH₂ by oxygen (**Fig. 1b**).

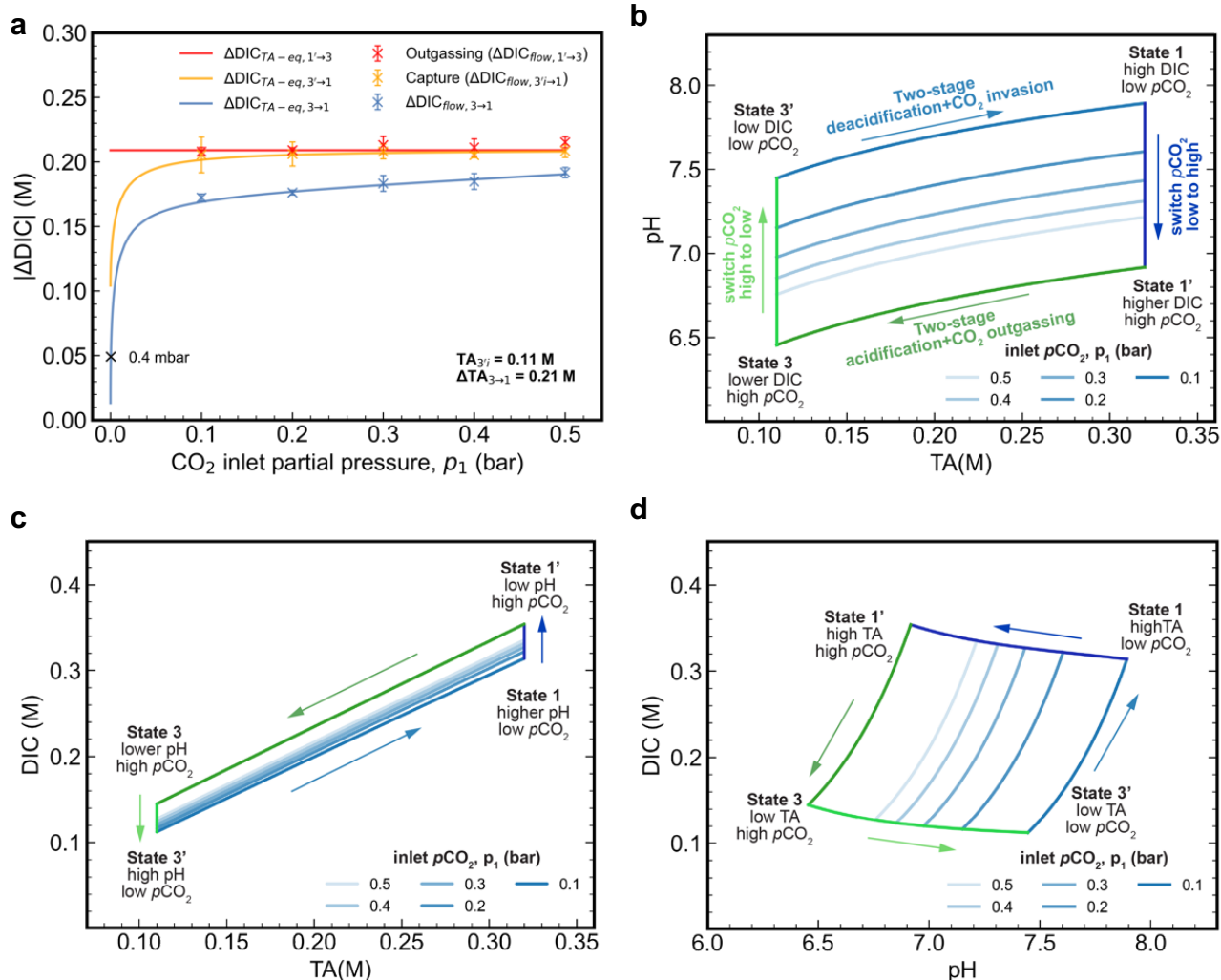


Fig. 4| Summary of the experimental concentrating cycles with different inlet $p\text{CO}_2$ in Fig. 3 and the TA/pH/DIC relations of the ideal cycles with corresponding experimental conditions. a, $\Delta\text{DIC}_{\text{flow}}$ extracted from Fig. 3 e and f (colored “x” markers) and calculated $\Delta\text{DIC}_{\text{TA-eq}}$ given $\text{TA}_{3\text{i}} = 0.11 \text{ M}$ and $\Delta\text{TA}_{3\rightarrow 1} = 0.21 \text{ M}$ (lines). The black “x” marker refers to the result that ΔDIC for the ideal cycle equals 0.049 M when $p\text{CO}_2 = 0.4 \text{ mbar}$. b, pH vs. TA in the ideal cycles, assuming $\text{TA}_{3\text{i}} = 0.11 \text{ M}$, $\Delta\text{TA}_{3\rightarrow 1} = 0.21 \text{ M}$ and gas-solution equilibrium. p_1 in the legends represents $p\text{CO}_2$ during the two-stage deacidification+ CO_2 invasion process. The arrows indicate the direction of the processes in the experiments. c, DIC vs. TA in the ideal cycles. d, DIC vs. pH in the ideal cycles.

Carbon Capture Cycles with $p_1 = 0.1 - 0.5 \text{ bar}$ at $20 - 150 \text{ mA cm}^{-2}$

The average CO_2 molar cycle work under 40 mA cm^{-2} is compared with those obtained under $20 - 150 \text{ mA cm}^{-2}$ (Fig. 5 a and ESI, Fig. S7). As current density increases at a fixed p_1 , the net cycle work increases as the required deacidification work increases and the acidification work returned decreases in magnitude; these trends are caused by increased ohmic, electron-transfer and mass-transport overpotentials at higher current density.²² It is noteworthy that we achieve $61.3 \text{ kJ mol}_{\text{CO}_2}^{-1}$ cycle work for $p_1 = 0.1 \text{ bar}$ and $p_3 = 1 \text{ bar}$ using a current density of 20 mA cm^{-2} , which is a competitive energy cost at a much higher current density compared to other electrochemical CO_2 separation methods for flue gas capture.^{24, 25} A linear extrapolation of the cycle work shows $57.1 \text{ kJ mol}_{\text{CO}_2}^{-1}$ at the low-current-density limit (Fig. 5e).

It is evident from **Fig. 5b** that $\Delta\text{DIC}_{\text{flow},3\rightarrow1}$ is independent of current density for a given value of p_1 . This occurs because varying current density changes only the rate of change in TA and not the value of $\Delta\text{TA}_{3\rightarrow1}$, and sufficient reaction time was allowed to approach gas-solution equilibrium, whether the current density was low (**Fig. 2f and g**) or high (**ESI, Fig. S8**). The slight variations in ΔTA and ΔDIC were caused by occasional foaming or negolyte droplets clinging to the wall of the reservoir, both of which cause small amounts of charge capacity to be instantaneously inaccessible from time to time. In contrast, increasing $p\text{CO}_2$ at the inlet raises $\Delta\text{DIC}_{\text{flow},3\rightarrow1}$ (**Fig. 5b**), for the reason explained in the discussion of Fig. 4d. In addition to the cycle results presented in **Fig. 5**, five cycles with $p_1 = 0.05$ bar and $p_3 = 1$ bar and current density being 40 mA cm^{-1} were tested under faster negolyte pumping to enhance mass transport rates, yielding an average cycle work of $92.6 \text{ kJ mol}_{\text{CO}_2}^{-1}$ (**ESI, Fig. S9**).

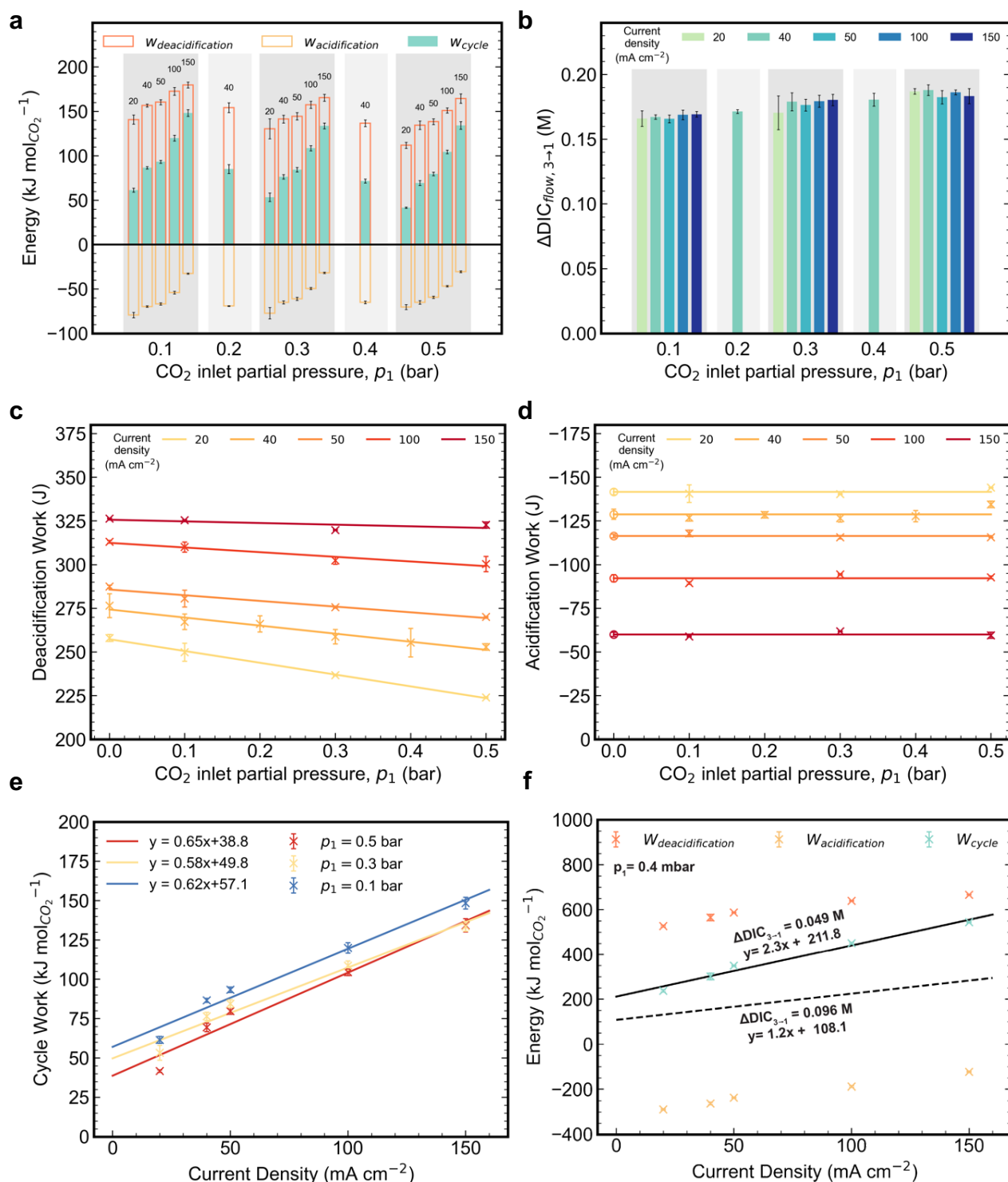


Fig. 5| Summary of the experimental concentrating cycles performed under 20, 40, 50, 100 and 150 mA cm^{-2} current densities and $p_1 = 0.5, 0.4, 0.3, 0.2$ and 0.1 bar. a, CO_2 molar deacidification, acidification and cycle work vs. p_1 for current densities indicated above the bars, in mA cm^{-2} . In both **a and **b** the horizontal axis is categorical, and each shadowed region refers to a single p_1 value. b, $\Delta\text{DIC}_{\text{flow}, 3 \rightarrow 1}$ vs p_1 for various current densities. c, Deacidification work vs. p_1 for various current densities. The “x” markers refer to measured data. The deacidification work of the cycles under pure N_2 is used for $p_1 = 0.0$ bar. d, Acidification work vs. p_1 for various current densities. The “x” markers refer to measured data. For each current density, the acidification work at $p_1 = 0.0$ bar (“o” markers) is chosen to be the average value of the work obtained at other p_1 values at the same current density. e, CO_2 molar deacidification,**

acidification and cycle work vs. current density for $p_1 = 0.1, 0.3$ and 0.5 bar. **f**, Estimated CO_2 molar deacidification, acidification and cycle work for $p_1 = 0.4$ mbar. Extrapolation is performed using deacidification and acidification work at 0.0 bar p_1 in **c** and **d**, and divided by expected $\Delta\text{DIC}_{3 \rightarrow 1}$ at $p_1 = 0.4$ mbar obtained from **Fig. 4d**. The solid line refers to a linear fit of CO_2 molar cycle work vs. current density assuming $\text{TA}_{3 \rightarrow 1} = 0.11$ M ($\Delta\text{DIC}_{3 \rightarrow 1} = 0.049$ M) and the dashed line refers to the same information but assuming $\text{TA}_{3 \rightarrow 1} = 0.0$ M ($\Delta\text{DIC}_{3 \rightarrow 1} = 0.096$ M).

Estimate of Molar Cycle Work at $p_1 = 0.4$ mbar and $p_3 = 1$ bar

Using the results obtained from $p_1 = 0.1 - 0.5$ bar, we estimate the CO_2 molar cycle work for $p_1 = 0.4$ mbar and $p_3 = 1$ bar, i.e. similar to DAC conditions. However, a simple regression of the molar cycle work from higher p_1 values to $p_1 = 0.4$ mbar does not guarantee accurate extrapolation because both deacidification work (**Fig. 5c**) and $\Delta\text{DIC}_{\text{flow},3 \rightarrow 1}$ vary as p_1 varies (**Fig. 4d**). Instead, we evaluate the molar cycle work at $p_1 = 0.4$ mbar using cycle work (**Fig. 5c** and **d**) and ideal cycle $\Delta\text{DIC}_{\text{TA-eq},3 \rightarrow 1}$, which we show corresponds closely to $\Delta\text{DIC}_{\text{flow},3 \rightarrow 1}$ at various p_1 . The deacidification work at $p_1 = 0.4$ mbar is simply the deacidification work under a pure N_2 atmosphere, i.e. 0.0 bar $p\text{CO}_2$ (**Fig. 5c**), and the reason that deacidification work decreases with higher p_1 is that higher p_1 lowers the average negolyte pH, which in turn decreases the cell voltage and thereby decreases the work (eq. 3). The acidification work is always the same because p_3 is always 1 bar and $\Delta\text{TA}_{3 \rightarrow 1}$ is always the same (hence the flat lines in **Fig. 5d**); therefore for $p_1 = 0.0$ bar we use the average work from higher p_1 values. With $\text{TA}_{3 \rightarrow 1} = 0.11$ M and $\Delta\text{TA}_{3 \rightarrow 1} = 0.21$ M, $\Delta\text{DIC}_{3 \rightarrow 1}$ at $p_1 = 0.4$ mbar and $p_3 = 1$ bar is 0.049 M (**Fig. 4d**). The molar cycle work for various current densities, evaluated by dividing the sum of deacidification and acidification work at $p_1 = 0.0$ bar by 0.049 M, is shown in **Fig. 5f**. A linear extrapolation through these values projects a minimum cycle work of $211.8 \text{ kJ molCO}_2^{-1}$ at the small-current-density limit (**Fig. 5f**). This is about 10% less energetic cost comparing with the concentrated KOH process.⁹ As shown by the dashed curve, however, with $\text{TA}_{3 \rightarrow 1} = 0.0$ M and the same $\Delta\text{TA}_{3 \rightarrow 1}$, the cycle work may be cut in half to $108.1 \text{ kJ molCO}_2^{-1}$; this occurs because of the nearly doubled $\Delta\text{DIC}_{\text{flow},3 \rightarrow 1}$ of 0.096 M despite similar cycle work (**ESI, Fig. S2 and S3**). In addition, due to its solubility of 0.7 M in aqueous solution,¹⁸ DSPZ can induce a $\Delta\text{TA}_{3 \rightarrow 1}$ or $\Delta[\text{OH}^-]$ of 1.4 M and thereby potentially yield even lower molar cycle work (**ESI, Fig. S4**)

Comparison with Existing Technologies

Table 2 summarizes some of the emerging technologies for point source capture, DAC, and direct ocean capture (DOC), where CO_2 is removed from seawater, allowing more CO_2 uptake by the ocean. Many approaches to DAC have used aqueous alkaline solutions^{2, 9} or solid amine-based adsorption methods,^{2, 24} which require thermal excursions to release captured CO_2 . One of the state-of-the-art DAC approaches relies on concentrated (2-5 Molar) alkaline solutions on a high-area contactor to absorb CO_2 and transform it into aqueous K_2CO_3 and KHCO_3 . These are then converted into solid CaCO_3 in a pellet reactor by mixing the aqueous carbonates with $\text{Ca}(\text{OH})_2$. Releasing the CO_2 requires heating the CaCO_3 to 900°C in an oxygen-fired calciner, which costs $264\text{--}296 \text{ kJ/molCO}_2$.^{2, 9} Another, less mature, aqueous approach uses amino acids for the carbon capture step and undergoes a subsequent sorbent regeneration cycle employing solid bis-iminoguanidine carbonate precipitation and CO_2 release through heating to $>100^\circ\text{C}$; this cycle requires $152\text{--}422 \text{ kJ/molCO}_2$, depending on the type of guanidine, because a significant portion of the energy contributes to removing the undesirable hydrate from guanidine carbonate crystal.^{10, 16} Solid sorbent DAC, mostly based on solid amine absorption and release through thermal and/or

pressure swing, allows reduced heating requirements (~ 100 °C), but the amines may decompose to volatile species that may damage the environment.²

Electrochemical carbon capture methods may offer solutions to overcome the high sorbent regeneration energy penalty and sorbent decomposition issues. Electrochemically mediated point source carbon capture methods^{7, 24, 26}, at low current densities, have exhibited lower energetic costs than amine-scrubbing methods. In addition, CO₂ removal from ocean water, which restores the CO₂ capture capability of oceans, via electrochemical methods such as bipolar membrane electrodialysis (BPMED), have shown promisingly low energetic cost.^{12, 13} However, the demonstrated works exhibited either low current density (slow kinetics) or low voltage efficiency. In addition, the high water-handling requirement of direct ocean capture adds significantly to the energetic cost.

The performance of our pH-swing flow cell, demonstrated for capture at 0.1 bar and projected for 0.4 mbar appears competitive compared with existing technologies, not only in terms of energetic cost with cheap electricity from renewable sources, but also because of much larger applicable current density (**Table 2**).²⁷ Additionally, the all-liquid configuration obviates the need for the precipitation and heating of solid carbonates. Furthermore, the compatibility with an aqueous electrolyte of non-volatile, non-corrosive and potentially low-cost organic molecules implies that a carbon capture technology based on this concept has the potential for wide scale practical implementation.

Table 2| Comparison of this work and emerging technologies for DAC, DOC and point source capture. CO₂ separation work with “th” subscript denote thermal energy inputs, whereas “e” subscript denotes electrical work input.

Method	Purpose	CO ₂ separation work inputs (kJ mol _{CO2} ⁻¹)	Current Density (mA cm ⁻²)
Alkaline solvent ^{2, 9}	DAC	264-396 _{th} ^a	N/A
Solid amine sorbents ²	DAC	150 – 211 _{th} ^b	N/A
Amino acid solvents and solid bis-aminoguanidines ¹⁰	DAC	152 – 422 _{th} ^c	N/A
Fuel cell concentrator ¹⁷	DAC	350 _e ^d	0.5
Processing seawater within a BPMED reactor ¹³	DOC	155 _e ^f	3.3
Titration seawater with BPMED acid/base ¹²	DOC	394 _e ^g	100
Traditional amine ab-/desorption ⁴	Point source capture	132 – 150 _{th}	N/A
Shell Cansolv ⁶	Point source capture	103 _{th}	N/A
Quinone Direct binding ⁷	Point source capture	56 _e ^h	0.5
EMAR ⁸	Point source capture	30 – 113 _e ⁱ	2.7 – 11.8
This work	0.1 bar capture	61 – 145_e	20 – 150

	0.4 mbar capture	108 – 212 _e	Small-current-density limit
--	------------------	------------------------	-----------------------------

^aWork input excludes electrical work required to operate air-liquid contactor, pellet reactor and auxiliary equipment.

^bDesorption energy for mid-range scenario; work input excludes electrical work required to operate air contactor fans and desorption vacuum pump.

^cEnergy required for bis(iminoguanidine) regeneration.

^dHydrogen gas is the energy source; Energy required to operate water cooling system is excluded.

^fWork input excludes costs for ocean water intake, pre-treatment and pumping.

^gEnergy consumption for the best-case acid process; Work input excludes electrical work required to operate pumps and chiller.

^hThe inlet gas source was simulated flue gas with 15% CO₂ and 3% O₂ in N₂, but exit partial pressure was ~0 bar. Note that the energy cost was calculated based on the amount of CO₂ absorbed, yet it is not clear that all absorbed CO₂ was released.

ⁱEnergy and current density values adopted from Fig.8(a) of ref.⁸ Simulated flue gas is 15% CO₂ in N₂.

Electrochemical Rebalancing

It is clearly difficult to avoid O₂ in either DAC or flue gas capture because the source gas contains 20% and 3–5% O₂, respectively. In the short term, the oxidation of DSPZH₂ by O₂ incurs an instantaneous loss in Coulombic efficiency. In the long term the cell will go out of balance, accumulating oxidized species in both electrolytes and TA₃^{·i}, KOH and DIC₃^{·i} in the negolyte (**Fig. 1b**).²³ As a result, ΔDIC_{3→1} will shrink without a concomitant decrease in cycle work (**ESI, Fig. S2b**), leading to an increase in CO₂ molar cycle work (**ESI, Fig. S2c**). Eventually the cell will no longer operate because both electrolytes are completely oxidized. As shown in **Fig. 6a** and **b**, as soon as the headspace was opened to air the Coulombic efficiency decreased to ~65%, and by the 20th subsequent cycle the cell lost all capacity due to depletion of reduced species, i.e. [K⁺]₄[Fe^{II}(CN)₆]⁴⁻, in the posolyte side. The negolyte pH also increased from near neutral to almost 14 during air exposure (**ESI, Fig. S11b**). Development of oxygen-insensitive molecules may alleviate the problem caused by oxygen, but even if a tiny amount of Coulombic efficiency loss, e.g. 0.1%, took place every cycle, the effect is cumulative and will eventually lead to an out-of-balance cell problem (**Fig. 1b**).

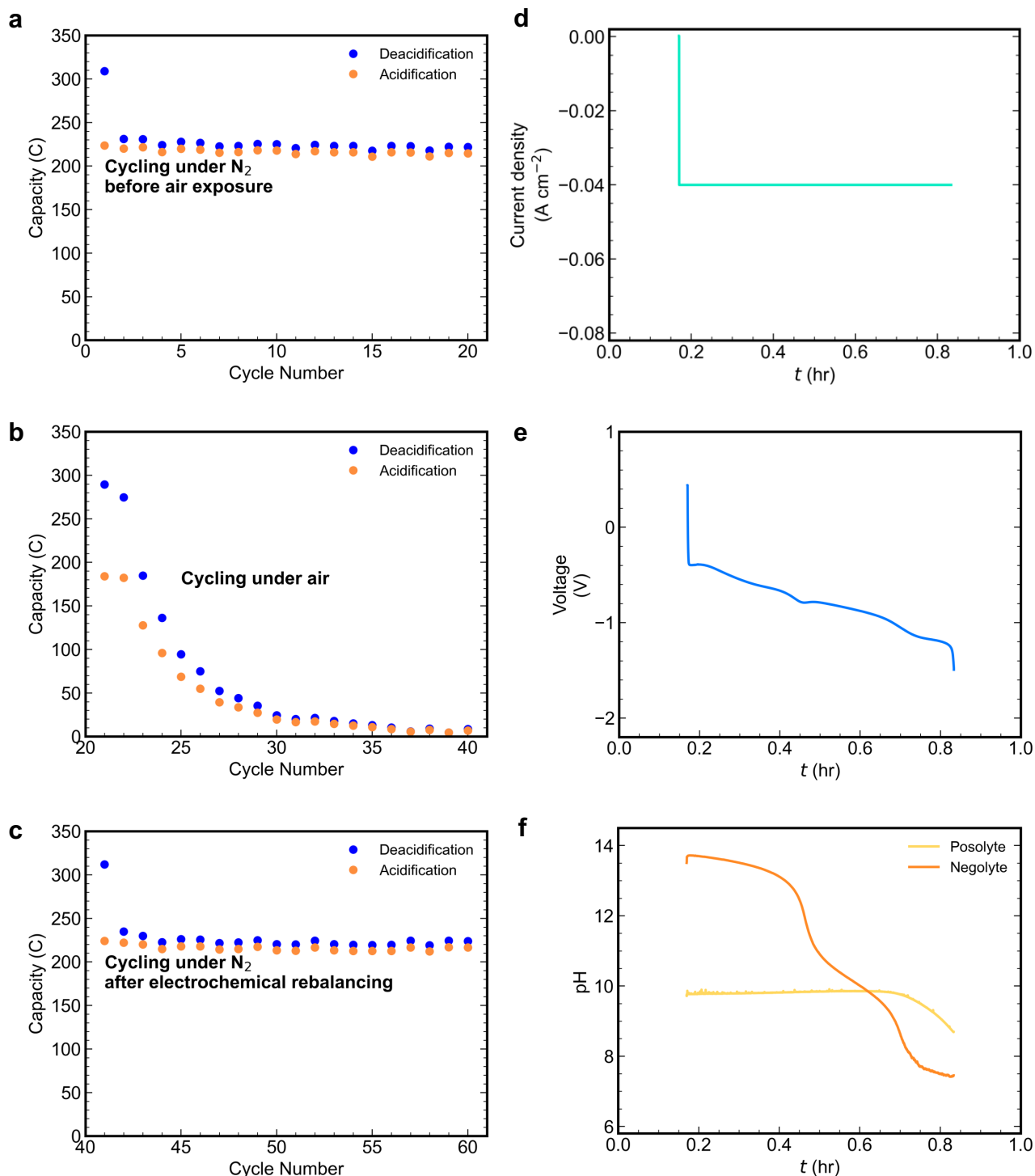


Fig. 6| The capacity fade caused by O_2 on $\text{Fe}(\text{CN})_6/\text{DSPZ}$ cell cycling (a,b,c) and its mitigation by the electrochemical rebalancing method (d,e,f). a, Charge capacity vs. cycle number of the cell under pure N_2 atmosphere. The first cycle has much higher deacidification capacity due to residual oxygen b, Charge capacity vs. cycle number of the same cell from a under air. Capacity fades quickly because of the depletion of $\text{K}_4\text{Fe}(\text{CN})_6$ in the posolyte. c, Charge capacity vs. cycle number of the cell from b under pure N_2 atmosphere, after the electrochemical rebalancing step. The first cycle has much higher deacidification capacity due to residual oxygen. d, Current density, e, voltage, f, Posolyte and negolyte pH during the electrochemical rebalancing step

Here we demonstrate the efficacy of the electrochemical rebalancing method. The method successfully recovers the pH of the negolyte and the capacity of the cell, which is thrown out-of-balance by O₂-induced side reactions. The electrochemical rebalancing process comprises the cathodic reaction $[K^+]_3[Fe^{III}(CN)_6]^{3-} + e^- \rightarrow [K^+]_4[Fe^{II}(CN)_6]^{4-}$ in the posolyte and the anodic oxygen evolution reaction, $OH^- \rightarrow 2e^- + \frac{1}{2}O_2$, in the negolyte. **Fig. 6d,e** and **f** show the cell behavior when the electrochemical rebalancing process is applied to the completely out-of-balance cell (**Fig. 6b**). The process starts when a constant current of -40 mA cm^{-2} is applied (**Fig. 6d**). The voltage immediately drops from 0.2 V to negative values because both the cathodic and anodic half reactions are at $\sim 0.4 \text{ V}$ vs. SHE at pH 14, and there is high activation overpotential for the oxygen evolution reaction (**Fig. 6e**). As the rebalancing process progresses, the pH of the negolyte side decreases (**Fig. 6f**), causing the anodic half reaction to shift to higher potential, thereby further decreasing the cell potential (**Fig. 6e**). The sharp drop in voltage to a plateau near 0.8 hours indicates the completion of the electrochemical rebalancing process. **Fig. 6c** shows the post-rebalancing cell capacity, which is almost identical to that prior to air exposure (**Fig. 6a**), indicating that essentially all lost capacity due to imbalance has been restored. The capacity accounting for all the electrons passed in the electrochemical rebalancing step is 476.8 C, which is within 1% of the theoretical capacity (473 C) of the posolyte side, suggesting a complete recovery of the K₄Fe(CN)₆ and minimal side reactions other than oxygen evolution. The posolyte pH did not change much during the process because the cathodic half-reaction is not proton-coupled (**Fig. 6f**). The neutral pH of the negolyte at the end of the process indicates that virtually all of the accumulated hydroxide has been removed (**Fig. 6f**). The undiminished capacity also suggests that this method is not detrimental to DSPZ. **Fig. S10** shows that the electrolytes, after electrochemical rebalancing, have the same carbon-capture capability as the original electrolytes. Hence, the electrochemical rebalancing process is a very effective method to remove the adverse effect of oxygen in DSPZ-based carbon capture flow cells. This method has potentially broad application beyond DSPZ and carbon capture, e.g. mitigating the oxygen effect in flow batteries with air or pH sensitive electrolytes (**ESI, More on Electrochemical Rebalancing**).^{23, 28-35} The overall energy cost is 378 J, which is approximately 1.4 times of the cost of one deacidification half cycle at 40 mA cm^{-2} (**Fig. 5c**). This will be a significant cost if the electrochemical rebalancing is applied every few cycles, which may be necessary for a DSPZ-based system for DAC, but if the negolyte molecule is much less air sensitive or the source gas has lower oxygen content, requiring electrochemical rebalancing less frequently than once every few tens of carbon capture/release cycles, the cost will be negligible. The development of oxygen-insensitive molecules for this purpose is the subject of active research.

Conclusion

In this work, we have performed a series of CO₂ concentrating cycles using a DSPZ-based flow cell with electrochemically induced pH swings, and the cycle work under different inlet partial pressures and current densities was analyzed and compared. We demonstrated a $61.3 \text{ kJ molCO}_2^{-1}$ cycle work for CO₂ separation for capture at $p_1 = 0.1 \text{ bar}$ and release at $p_3 = 1 \text{ bar}$, at a current density of 20 mA cm^{-2} . If TA_{3:1} is carefully maintained at a low level the projected separation work for $p_1 = 0.4 \text{ mbar}$ and $p_3 = 1 \text{ bar}$, in the low current limit, is $108.1 \text{ kJ molCO}_2^{-1}$, and this figure can be further lowered if a higher concentration of DSPZ or another PCET-active molecule is used. Recognizing the inevitable O₂-induced imbalance and capacity fade in both point source capture and DAC, we report an electrochemical rebalancing method that recovers the initially healthy cell

composition. This method can serve as a convenient tool for mitigating oxygen-related problems in many electrochemical applications. We anticipate that the low energetic cost of the pH swing cycles and the effectiveness of the oxygen mitigation method demonstrated here will accelerate the techno-economic competitiveness of electrochemically-driven carbon capture systems.

Methods

Materials and characterization

All chemicals were purchased from Sigma-Aldrich or Acros Organics and were used as received. The synthetic method for DSPZ is adapted from previous work.¹⁸ In this work, sodium hydride was used to deprotonate the reaction intermediate phenazine-2,3-diol (DHPZ) instead of sodium methoxide.

Flow cell experiments

Flow cell experiments were constructed with cell hardware from Fuel Cell Tech. (Albuquerque, NM), assembled into a zero-gap flow cell configuration, similar to a previous report.¹⁸ Pyrosealed POCO graphite flow plates with serpentine flow patterns were used for both electrodes. Each electrode comprised a 5 cm² geometric surface area covered by a stack of four sheets of Sigracet SGL 39AA porous carbon paper pre-baked in air for 24 h at 400 °C. The outer portion of the space between the electrodes was gasketed by Viton sheets with the area over the electrodes cut out. Torque applied during cell assembly was 80 lb-in on each of eight 1/4-28 bolts. The membrane used is a Fumasep E620(K) cation exchange membrane. Cell electrolytes comprised 10 mL 0.11 M DSPZ in 1 M KCl (negolyte, capacity limiting, theoretical capacity 212 C) and 35 mL 0.1 M K₄Fe(CN)₆ and 0.04 M K₃Fe(CN)₆ in 1 M KCl (posolyte, non-capacity limiting, theoretical capacity 473 C). For every new CO₂ capture cycle condition (changing current density or inlet *p*CO₂), the posolyte was replaced with a fresh solution and the negolyte was acidified by adding drops of 1 M HCl to remove the accumulating effect of oxygen side reactions. 10 µL of antifoam B emulsion purchased from Sigma-Aldrich was added into the negolyte solution before cell cycling to suppress foam formation. Posolytes were fed into the cell through fluorinated ethylene propylene (FEP) tubing at a rate of 100 mL min⁻¹ controlled by a Cole-Parmer Masterflex L/S peristaltic pump, and the negolytes were circulated at the same rate controlled by a Cole-Parmer Masterflex digital benchtop gear pump system. Both posolyte and negolyte upstream gas was controlled by Sierra Smart Trak 50 Mass Flow Controllers. The flowmeter used in the downstream of negolyte headspace was a Servoflo FS4001-100-V-A. The CO₂ sensor was an ExplorIR-W 100% CO₂ sensor purchased from co2meter.com. A Mettler Toledo pH electrode LE422 was used to monitor electrolyte pH. As shown in **Fig. 1 a**, a drierite drying tube (Cole Parmer) was placed in between the sensors and the negolyte chamber to reduce humidity level of the gas.

Glassy carbon (BASi MF-2012, 3.0mm diameter) was used as the working electrode for all three-electrode CV tests. A Ag/AgCl reference electrode (BASi MF-2052, pre-soaked in 3 M NaCl solution), and a graphite counter electrode were used for CV tests. CV tests and cell cycling were performed using a Gamry Reference 3000 potentiostat. All cycles were galvanostatic until the 1.65 V and 0.2 V voltage cutoff for deacidification and acidification, respectively, were reached, and then went through a potentiostatic process until the current reached 10 mA cm⁻². In the CO₂ cycles with *p*₁ = 0.1, 0.2, 0.3, 0.4, and 0.5 bar, the MFCs set the initial negolyte headspace atmosphere to be *p*₁, which was then switched back and forth between *p*₁ and *p*₃ every three hours. In the cycles with *p*₁ = 0.05 bar, the switching period was five hours.

Calculation of absorbed or released CO₂ amount

Because the deviation from baseline in **Fig. 2 g** is solely caused by CO₂ absorption, the amount of CO₂ captured is calculated by integrating over the difference between the recorded flow rate and the baseline in between 0.2 and 1.8 hours, i.e.

$$Q_{CO_2} = \sum_{n=t_i}^{t_f} (\dot{V}^{base} - \dot{V}^n) \Delta t \quad (1)$$

where Q_{CO_2} is the volume of CO_2 , t_i is the start time, t_f is the final time, V^n is the instantaneous volumetric flow rate at n^{th} data recording time t_n , V^{base} is the baseline flow rate of 11.6 mL min^{-1} , and Δt is the time difference between successive measurements.

Calculation of deacidification, acidification and cycle work

The net cycle work is calculated by combining the work required for deacidification in process $3' \rightarrow 1$ and the work returned by acidification in process $1' \rightarrow 3$, i.e.

$$w_{cycle} = w_{deacidification} + w_{acidification} \quad (2)$$

The work in a process is calculated by summing over the product of voltage (Fig. 2 a) and current (Fig. 2 b), i.e.

$$w_{deacidification/acidification} = \sum_{n=t_i}^{t_f} V^n j^n A \Delta t \quad (3)$$

where V^n is the cell voltage at the n^{th} data recording time t^n , j^n is the current density at t^n and A is the active geometric area of 5 cm^2 .

The molar cycle work \bar{w} is calculated by dividing w_{cycle} by $-\Delta DIC_{flow,1 \rightarrow 3}$ or $\Delta DIC_{flow,3 \rightarrow 1}$:

$$\bar{w} = \frac{w_{cycle}}{\Delta DIC_{flow,3 \rightarrow 1}} \quad (4)$$

where $\Delta DIC_{flow,1 \rightarrow 3} = \Delta DIC_{TA-pH,1 \rightarrow 1'} + \Delta DIC_{flow,1' \rightarrow 3}$ and $\Delta DIC_{flow,3 \rightarrow 1} = \Delta DIC_{flow,3' \rightarrow 1} + \Delta DIC_{TA-pH,3 \rightarrow 3'f}$. For high current densities (100 and 150 mA cm^{-2}), we use $\Delta DIC_{TA-eq,1 \rightarrow 1'}$ and $\Delta DIC_{TA-eq,3 \rightarrow 3'f}$ instead of $\Delta DIC_{TA-pH,1 \rightarrow 1'}$ and $\Delta DIC_{TA-pH,3 \rightarrow 3'f}$, respectively, because of an artifact in the pH measurement at high current density, tentatively attributed to crosstalk between potentiation lines. We explain in the main text that ΔDIC_{TA-pH} and ΔDIC_{TA-eq} are interchangeable when the pH measurement is valid.

Data availability: The data and code that support the plots and discussion of this study are available from the corresponding author upon reasonable request.

Conflicts of interest

None.

Acknowledgments

This research was supported by a grant from the Harvard University Climate Change Solutions Fund. We thank Daniel Schrag, Robert Gustafson, Anatoly Rinberg, Andrew Bergman, Tommy George and Eric Fell for helpful discussions.

References

1. Raupach, M. R.; Marland, G.; Ciais, P.; Le Quere, C.; Canadell, J. G.; Klepper, G.; Field, C. B., Global and regional drivers of accelerating CO₂ emissions. *Proc Natl Acad Sci U S A* **2007**, *104* (24), 10288-93.
2. *Negative Emissions Technologies and Reliable Sequestration: A Research Agenda* (2019). The National Academies Press: 2019.
3. Annual Energy Outlook 2020 with projections to 2050. DOE, Ed. www.eia.gov/aeo, 2020.
4. Goto, K.; Kodama, S.; Higashii, T.; Kitamura, H., Evaluation of Amine-Based Solvent for Post-Combustion Capture of Carbon Dioxide. *J Chem Eng Jpn* **2014**, *47* (8), 663-665.
5. Li, K.; Cousins, A.; Yu, H.; Feron, P.; Tade, M.; Luo, W.; Chen, J., Systematic study of aqueous monoethanolamine-based CO₂ capture process: model development and process improvement. *Energy Science & Engineering* **2016**, *4* (1), 23-39.
6. Singh, A.; Stéphenne, K., Shell Cansolv CO₂ capture technology: Achievement from First Commercial Plant. *Energy Procedia* **2014**, *63*, 1678-1685.
7. Liu, Y.; Ye, H. Z.; Diederichsen, K. M.; Van Voorhis, T.; Hatton, T. A., Electrochemically mediated carbon dioxide separation with quinone chemistry in salt-concentrated aqueous media. *Nat Commun* **2020**, *11* (1), 2278.
8. Wang, M.; Herzog, H.; Hatton, T. A., CO₂ Capture Using Electrochemically Mediated Amine Regeneration. *Industrial & Engineering Chemistry Research* **2020**, *59*, 7087-7096.
9. Keith, D. W.; Holmes, G.; St. Angelo, D.; Heidel, K., A Process for Capturing CO₂ from the Atmosphere. *Joule* **2018**, *2* (8), 1573-1594.
10. Brethomé, F. M.; Williams, N. J.; Seipp, C. A.; Kidder, M. K.; Custelcean, R., Direct air capture of CO₂ via aqueous-phase absorption and crystalline-phase release using concentrated solar power. *Nat Energy* **2018**, *3* (7), 553-559.
11. Sanz-Perez, E. S.; Murdock, C. R.; Didas, S. A.; Jones, C. W., Direct Capture of CO₂ from Ambient Air. *Chem Rev* **2016**, *116* (19), 11840-11876.
12. de Lannoy, C.-F.; Eisaman, M. D.; Jose, A.; Karnitz, S. D.; DeVaul, R. W.; Hannun, K.; Rivest, J. L. B., Indirect ocean capture of atmospheric CO₂: Part I. Prototype of a negative emissions technology. *Int J Greenh Gas Con* **2018**, *70*, 243-253.
13. Digdaya, I. A.; Sullivan, I.; Lin, M.; Han, L.; Cheng, W. H.; Atwater, H. A.; Xiang, C., A direct coupled electrochemical system for capture and conversion of CO₂ from oceanwater. *Nat Commun* **2020**, *11* (1), 4412.
14. Lail, M.; Tanthana, J.; Coleman, L., Non-Aqueous Solvent (NAS) CO₂ Capture Process. *Energy Procedia* **2014**, *63*, 580-594.
15. Heldebrant, D. J.; Koech, P. K.; Glezakou, V.-A.; Rousseau, R.; Malhotra, D.; Cantu, D. C., Water-Lean Solvents for Post-Combustion CO₂ Capture: Fundamentals, Uncertainties, Opportunities, and Outlook. *Chemical Reviews* **2017**, *117*, 9594-9624.
16. Custelcean, R.; Williams, N. J.; Wang, X.; Garrabrant, K. A.; Martin, H. J.; Kidder, M. K.; Ivanov, A. S.; Bryantsev, V. S., Dialing in Direct Air Capture of CO₂ by Crystal Engineering of Bisiminoguanidines. *ChemSusChem* **2020**, *13*, 6381-6390.
17. Eisaman, M.; Schwartz, D.; Amic, S.; Larner, D.; Zesch, J.; Torres, F.; Littau, K. In *Energy-efficient electrochemical CO₂ capture from the atmosphere*, Technical Proceedings of the 2009 Clean Technology Conference and Trade Show, 2009; pp 3-7.

- 554 18. Jin, S.; Wu, M.; Gordon, R. G.; Aziz, M. J.; Kwabi, D. G., pH swing cycle for CO₂
555 capture electrochemically driven through proton-coupled electron transfer. *Energy &*
556 *Environmental Science* **2020**, *13* (10), 3706-3722.
- 557 19. Xie, H.; Wu, Y.; Liu, T.; Wang, F.; Chen, B.; Liang, B., Low-energy-consumption
558 electrochemical CO₂ capture driven by biomimetic phenazine derivatives redox medium. *Applied*
559 *Energy* **2020**, 259.
- 560 20. Xie, H.; Jiang, W.; Liu, T.; Wu, Y.; Wang, Y.; Chen, B.; Niu, D.; Liang, B., Low-
561 Energy Electrochemical Carbon Dioxide Capture Based on a Biological Redox Proton Carrier.
562 *Cell Reports Physical Science* **2020**, *1* (5).
- 563 21. Zeebe, R. E.; Wolf-Gladrow, D., *CO₂ in Seawater: Equilibrium, Kinetics, Isotopes*.
564 Elsevier: Amsterdam, 2005; Vol. 65.
- 565 22. Chen, Q.; Gerhardt, M. R.; Aziz, M. J., Dissection of the Voltage Losses of an Acidic
566 Quinone Redox Flow Battery. *Journal of the Electrochemical Society* **2017**, *164* (6), A1126-
567 A1132.
- 568 23. Goulet, M.-A.; Aziz, M. J., Flow Battery Molecular Reactant Stability Determined by
569 Symmetric Cell Cycling Methods. *Journal of the Electrochemical Society* **2018**, *165* (7), A1466-
570 A1477.
- 571 24. Renfrew, S. E.; Starr, D. E.; Strasser, P., Electrochemical Approaches toward CO₂ Capture
572 and Concentration. *ACS Catalysis* **2020**, *10* (21), 13058-13074.
- 573 25. Kang, J. S.; Kim, S.; Hatton, T. A., Redox-responsive sorbents and mediators for
574 electrochemically based CO₂ capture. *Current Opinion in Green and Sustainable Chemistry* **2021**,
575 *31*, 100504.
- 576 26. Voskian, S.; Hatton, T. A., Faradaic electro-swing reactive adsorption for CO₂ capture.
577 *Energy & Environmental Science* **2019**.
- 578 27. Sharifian, R.; Wagterveld, R. M.; Digdaya, I. A.; Xiang, C.; Vermaas, D. A.,
579 Electrochemical carbon dioxide capture to close the carbon cycle. *Energy & Environmental*
580 *Science* **2021**.
- 581 28. Jin, S.; Jing, Y.; Kwabi, D. G.; Ji, Y.; Tong, L.; De Porcellinis, D.; Goulet, M. A.;
582 Pollack, D. A.; Gordon, R. G.; Aziz, M. J., A water-miscible quinone flow battery with high
583 volumetric capacity and energy density. *ACS Energy Letters* **2019**, *4* (6), 1342-1348.
- 584 29. Ji, Y.; Goulet, M. A.; Pollack, D. A.; Kwabi, D. G.; Jin, S.; Porcellinis, D.; Kerr, E. F.;
585 Gordon, R. G.; Aziz, M. J., A Phosphonate-Functionalized Quinone Redox Flow Battery at Near-
586 Neutral pH with Record Capacity Retention Rate. *Advanced Energy Materials* **2019**, *9* (12),
587 1900039.
- 588 30. Beh, E. S.; De Porcellinis, D.; Gracia, R. L.; Xia, K. T.; Gordon, R. G.; Aziz, M. J., A
589 Neutral pH Aqueous Organic-Organometallic Redox Flow Battery with Extremely High Capacity
590 Retention. *ACS Energy Letters* **2017**, *2* (3), 639-644.
- 591 31. Jin, S.; Fell, E. M.; Vina-Lopez, L.; Jing, Y.; Michalak, P. W.; Gordon, R. G.; Aziz, M.
592 J., Near Neutral pH Redox Flow Battery with Low Permeability and Long-Lifetime Phosphonated
593 Viologen Active Species. *Advanced Energy Materials* **2020**, *10* (20), 2000100.
- 594 32. Kwabi, D. G.; Lin, K.; Ji, Y.; Kerr, E. F.; Goulet, M.-A.; De Porcellinis, D.; Tabor, D.
595 P.; Pollack, D. A.; Aspuru-Guzik, A.; Gordon, R. G.; Aziz, M. J., Alkaline quinone flow battery
596 with long lifetime at pH 12. *Joule* **2018**, *2* (9), 1907-1908.
- 597 33. Hu, B.; DeBruler, C.; Rhodes, Z.; Liu, T. L., Long-Cycling Aqueous Organic Redox Flow
598 Battery (AORFB) toward Sustainable and Safe Energy Storage. *J Am Chem Soc* **2017**, *139* (3),
599 1207-1214.

- 600 34. Huang, C. L.; Liu, C. J.; Wu, K. J.; Yue, H. R.; Tang, S. Y.; Lu, H. F.; Liang, B., CO₂
601 Capture from Flue Gas Using an Electrochemically Reversible Hydroquinone/Quinone Solution.
602 *Energ Fuel* **2019**, 33 (4), 3380-3389.
- 603 35. Ulaganathan, M.; Aravindan, V.; Yan, Q.; Madhavi, S.; Skyllas-Kazacos, M.; Lim, T.
604 M., Recent Advancements in All-Vanadium Redox Flow Batteries. *Advanced Materials Interfaces*
605 **2016**, 3 (1), 1500309.
606

1 **Electronic Supplementary Information**

2
3 *for*

4
5 **Low Energy Carbon Capture via Electrochemically Induced pH Swing with**
6 **Electrochemical Rebalancing**

7
8 Shijian Jin[†], Min Wu[†], Yan Jing[‡], Roy Gordon[‡] and Michael J. Aziz^{†*}

9
10 [†] John A. Paulson School of Engineering and Applied Sciences, Harvard University, Cambridge,
11 Massachusetts, 02138, United States

12
13 [‡]Department of Chemistry and Chemical Biology, Harvard University, Cambridge,
14 Massachusetts 02138, United States

15
16 *maziz [at] harvard [dot] edu
17

Table of Sections

1 CO ₂ Molar Ideal Cycle Work	5
2 Cycle Data.....	10
3 More on Electrochemical Rebalancing	15

Table of Additional Figures

Fig. S 1 Ideal cycles constructed using $p_1 = 0.4$ mbar and $p_3 = 1$ bar, $\Delta TA_{3 \rightarrow 1} = 0.21$ M and varying $TA_{3'}$. a-c, $TA_{3'} = 0.0$ M; d-f, $TA_{3'} = 0.11$ M and g-i, $TA_{3'} = 0.21$ M;.....	7
Fig. S 2 Dependence of (a) $w_{\text{cycle,ideal}}$, (b) $\Delta DIC_{TA-pH,3 \rightarrow 1}$ (c) and \bar{w}_{ideal} on $TA_{3'}$ in the ideal cycles with $p_1 = 0.4$ mbar, and $p_3 = 1$ bar, $\Delta TA_{3 \rightarrow 1} = 0.21$ M.	8
Fig. S 3 Dependence of (a) $w_{\text{cycle,ideal}}$, (b) $\Delta DIC_{TA-eq,3 \rightarrow 1}$ and (c) \bar{w}_{ideal} on p_1 in the ideal cycles with $\Delta TA_{3 \rightarrow 1} = 0.21$ M and $TA_{3'} = 0.0, 0.11$ and 0.21 M. The 'x' marks indicate $p_1 = 0.4$ mbar. .	8
Fig. S 4 Dependence of (a) $w_{\text{cycle,ideal}}$, (b) $\Delta DIC_{TA-eq,3 \rightarrow 1}$ and (c) and \bar{w}_{ideal} on $\Delta TA_{3 \rightarrow 1}$ in the ideal cycles with $p_1 = 0.4$ mbar, $p_3 = 1$ bar and $TA_{3'} = 0.0$ M.	8
Fig. S 5 Duration of the CO ₂ capture and release processes in the cycles with 40 mA cm^{-2} current density. a, Downstream pCO_2 of one capture half cycle for each of the inlet pCO_2 conditions. b, Filtered total gas flow rate of one outgassing half cycle for each of the inlet pCO_2 conditions. All the processes look identical because of the same exit condition, so an arbitrary offset is added to differentiate the curves.....	10
Fig. S 6 Capture and outgassing durations extracted from Fig. S 5 a and b.	10
Fig. S 7 Eighty-five CO ₂ concentrating cycles with varying inlet pCO_2 and current densities. These are the raw data for Fig. 5. Same cell was used as in Fig 2. Liquid pumping rate is 50 mL min^{-1} for all the cycles. Note that, the pH measurements for high current densities are inaccurate, as the pH should never be able to reach $pH > 14$ for 0.11 M DSPZ . a, Current density. b, Voltage. c, N ₂ and CO ₂ percentage in the upstream source gas, controlled by mass flow controllers. d, CO ₂ partial pressure. e, Total gas flow rate.	11
Fig. S 8 One CO ₂ concentrating cycle from Fig. S 7 with 0.1 bar inlet pCO_2 and 1 bar exit pCO_2 at 150 mA cm^{-2} . Note that, the pH measurements are not shown because of an inexplicable artifact only present at high current, so it is invalid to extract DIC_{TA-pH} for this condition. However, DIC_{TA-eq} can be extracted because sufficient gas-solution is reached, as demonstrated by fact that the pCO_2 and flow curves return to their baselines after CO ₂ invasion and outgassing. a, Voltage profile. b, Current density. c, N ₂ and CO ₂ percentage in the upstream source gas, controlled by MFC. d, CO ₂ partial pressure. e, Total gas flow rate.....	12

63	Fig. S 9 Five CO ₂ concentrating cycles with 0.05 bar inlet $p\text{CO}_2$ and 1 bar exit $p\text{CO}_2$ at 40 mA	
64	cm ⁻² . Same cell was used as in Fig. 2. Fresh negolyte and posolyte were used. The liquid pumping	
65	rate is 150 mL min ⁻¹ , which is 50% faster than for capture at higher inlet pressure. a, Voltage	
66	profile. b, Current density. c, pH of the negolyte. d, N ₂ and CO ₂ percentage in the upstream source	
67	gas, controlled by mass flow controllers. e, CO ₂ partial pressure. f, Total gas flow rate.	13
68		
69	Fig. S 10 Post-electrochemical rebalancing CO ₂ capture with 0.05 bar inlet $p\text{CO}_2$ and 1 bar exit	
70	$p\text{CO}_2$ at 40 mA cm ⁻² . Same cell was used as in Fig.2. Same posolyte and negolyte as in Fig. S 9	
71	were used. The liquid pumping rate is 150 mL min ⁻¹ . a, Voltage profile. b, Current density. c, pH	
72	of the negolyte. d, N ₂ and CO ₂ percentage in the upstream source gas, controlled by mass flow	
73	controllers. e, CO ₂ partial pressure. f, Total gas flow rate. The system has the same carbon	
74	capture/release capability after the post-electrochemical rebalancing.	14
75		
76	Fig. S 11 pH of the negolyte during cycles before air exposure (a), under air (b) and after	
77	electrochemical rebalancing (c), respectively. pH drifts up because of oxygen presence.	15
78		
79	Fig. S 12 Cyclic voltammetry of DSPZ and 1 M KOH background. No additional peak was	
80	observed for DSPZ during the oxidative scan, indicating absence of side reactions.	15

83
84 **Table S 1| Table of acronyms**

Acronyms	Explanation
BPMED	bipolar membrane electrodialysis
CEM	cation exchange membrane
DAC	direct air capture
DIC	dissolved inorganic carbon
DIC _x	concentration of dissolved inorganic carbon in state “x”
$\Delta\text{DIC}_{\text{flow},x\rightarrow y}$	change in DIC between states “x” and “y” ($\text{DIC}_y - \text{DIC}_x$), measured by flow meter and CO ₂ sensor
$\Delta\text{DIC}_{\text{TA-pH},x\rightarrow y}$	change in DIC between states “x” and “y” ($\text{DIC}_y - \text{DIC}_x$), measured by known total alkalinity and measured pH
$\Delta\text{DIC}_{\text{TA-eq},x\rightarrow y}$	change in DIC between states “x” and “y” ($\text{DIC}_y - \text{DIC}_x$), measured by by known total alkalinity and assuming gas-solution equilibrium
DOC	direct ocean capture
DSPZ	sodium 3,3'-(phenazine-2,3-diylbis(oxy))bis(propene-1-sulfonate)
DSPZH ₂	reduced DSPZ
EMAR	electrochemically mediated amine regeneration
K ₃ Fe(CN) ₆	potassium ferricyanide (oxidized form of Fe(CN) ₆)
K ₄ Fe(CN) ₆	potassium ferrocyanide (reduced form of Fe(CN) ₆)
MFC	mass flow controller
p_1	CO ₂ partial pressure in bar during CO ₂ capture (inlet)
p_3	CO ₂ partial pressure in bar during CO ₂ outgassing (exit)
PCET	proton-coupled electron transfer
pH _{mea}	pH measured by pH probe
pH _{TA-eq}	pH calculated using known total alkalinity and assuming gas-solution equilibrium
TA	total alkalinity
TA _x	concentration of total alkalinity in state “x”
$\Delta\text{TA}_{x\rightarrow y}$	change in TA between states “x” and “y” ($\text{TA}_y - \text{TA}_x$), measured by counting charges during deacidification or acidification, which is equivalent to twice the concentration of DSPZ.

1 CO₂ Molar Ideal Cycle Work

For a system with given $TA_{3,i}$ and $\Delta TA_{3 \rightarrow 1}$, i.e. DSPZ concentration, the ideal cycle work is defined as the work input for driving the system through electrochemical deacidification at p_1 and a subsequent electrochemical acidification at p_3 , at an infinitesimal current. In the ideal cycle, gas-solution equilibrium is assumed at every point and because TA is known, pH_{TA-eq} and DIC_{TA-eq} at every point can be calculated. The CO₂ molar ideal cycle work, which we denote as \bar{w}_{ideal} , is obtained from dividing the ideal cycle work by expected $\Delta DIC_{3 \rightarrow 1}$, i.e. $\Delta DIC_{TA-eq, 3 \rightarrow 1}$.

This section explains how \bar{w}_{ideal} is calculated in detail. Both of the ideal cycle work and $\Delta DIC_{TA-eq, 3 \rightarrow 1}$ are governed by these parameters: initial TA ($TA_{3,i}$ or simply TA_3 , because $TA_{3,i}$ and $TA_{3,f}$ will be the same in an ideal cycle), $\Delta TA_{3 \rightarrow 1}$ and pCO_2 at p_1 , and the following equations:

$$DIC = [CO_2(aq)] + [HCO_3^-] + [CO_3^{2-}]; \quad (1)$$

$$K_1 = \frac{[HCO_3^-][H^+]}{[CO_2(aq)]}; \quad (2)$$

$$K_2 = \frac{[CO_3^{2-}][H^+]}{[HCO_3^-]}; \quad (3)$$

$$TA \equiv [OH^-] + [HCO_3^-] + 2[CO_3^{2-}] - [H^+]; \quad (4)$$

$$[S^+] - [S^-] = TA; \quad (5)$$

$$[H^+][OH^-] = 10^{-14}, \quad (6)$$

where the K_1 and K_2 used here are 1.1×10^{-6} M and 4.1×10^{-10} M,¹ resulting in the first and second pK_a for carbonic acid being 6.0 and 9.4, respectively. Eq. S4 is the definition of TA of the solution under consideration and eq. S5 arises from the charge neutrality constraint in solution (S^+ and S^- correspond to the cationic and anionic species of the electrolyte salt). During deacidification, $[S^+]$ increases in the negolyte reservoir, so TA increases as well (eq. S5), which means an increase of hydroxide concentration or $[HCO_3^-]$ or $[CO_3^{2-}]$ given nonzero pCO_2 (eq. S4). The reverse happens during acidification. The expressions for the concentration of each constituent of DIC can be derived by rearranging the above equations:

$$[CO_2(aq)] = \frac{DIC}{1 + \frac{K_1}{[H^+]} + \frac{K_1 K_2}{[H^+]^2}}; \quad (7)$$

$$[HCO_3^-] = \frac{DIC}{1 + \frac{[H^+]}{K_1} + \frac{K_2}{[H^+]}}; \quad (8)$$

$$[\text{CO}_3^{2-}] = \frac{\text{DIC}}{1 + \frac{[\text{H}^+]}{K_2} + \frac{[\text{H}^+]^2}{K_1 K_2}}; \quad (9)$$

TA_{3'} is calculated using eq. S7, measured pH and assumed gas-solution equilibrium, i.e.

$$[\text{CO}_2(\text{aq})] = 0.035 \times p\text{CO}_2. \quad (10)$$

where 0.035 comes from Henry's Law constant of 35 mM bar⁻¹ at room temperature and the units of [CO₂(aq)] and pCO₂ are Molar and bars, respectively. For example, in **Table 1**, pH_{meas} at state 3'_i was 7.4, and pCO₂ was 0.1 bar, so DIC can be derived from eq. S7 and S10, and subsequently [HCO₃⁻] and [CO₃²⁻] from eq. S8 and S9, respectively. TA_{3'} is then obvious from eq. S4. Because ΔTA_{3'_i→1}, which is determined by the concentration of DSPZ, is equal to ΔTA_{3→1}, and -ΔTA_{1'→3} (or -ΔTA_{1→3}) in the ideal cycle, TA at states 1, 1' and 3 can be derived from TA_{3'} and ΔTA values. Because TA and pCO₂ is known for each state, pH_{TA-eq} and DIC_{TA-eq} can be calculated. Then ΔDIC_{TA-eq,3'→1} is simply DIC_{TA-eq,1} minus DIC_{TA-eq,3}. In fact, we can calculate TA, pH_{TA-eq} and DIC_{TA-eq} of every point in between the states as well, and hence construct the ideal cycles. Because of the 2H⁺/2e⁻ redox processes of DSPZ,² its reduction potential, and overall cell potential decreases 59 mV for every unit of increase in pH. This allows us to calculate the ideal cycle work using the following equation:

$$w_{\text{cycle,ideal}} = \sum_{n=1} 0.059 \times (pH_{\text{deacidification}}(TA(n)) - pH_{\text{acidification}}(TA(n))) \times \Delta TA \times F \quad (11)$$

Where *n* is the index, TA increases by ΔTA Molar when *n* increases by 1, pH is a function of TA and the process, 0.059 (V/pH) is the conversion factor between pH and cell voltage, *F* is the Faraday constant (96485 C mol⁻¹) and the unit of *w*_{cycle,ideal} is J L⁻¹. Then *w*_{ideal} follows naturally by dividing *w*_{cycle,ideal} by ΔDIC_{3→1}.

$$\bar{w}_{\text{ideal}} = \frac{w_{\text{cycle,ideal}}}{\Delta \text{DIC}_{\text{TA-eq},3 \rightarrow 1}} \quad (12)$$

As mentioned in the main text, ΔDIC values vary as *p*₁, TA_{3'} and ΔTA_{3→1} change. **Fig. 4 e, f and g** show the ideal cycles for various *p*₁ given fixed *p*₃, TA_{3'} and ΔTA_{3→1}. The amount of CO₂ captured in process 3'_i→1 and monitored by the flow meter and the CO₂ sensor is around 50 mL, which translates to 0.21 M ΔDIC_{flow,3'_i→1}, assuming *T* = 293 K and *p* = 1 bar, across all different *p*₁ values (**Fig. 4a**). This similarity is consistent with the ideal cycle behavior, illustrated in **Fig. 4 c** and the alignment of measured ΔDIC_{flow,3'_i→1} with the theoretical ΔDIC_{TA-eq,3'→1} vs. pCO₂ curve. The similar amount of CO₂ captured and released, i.e. ΔDIC_{flow,3'_i→1} and ΔDIC_{flow,1'→3}, is caused by the coincidental resemblance of the slopes of the two-stage deacidification+CO₂ invasion and the two-stage acidification+CO₂ outgassing processes under the experimental conditions (**Fig. 4 c**). The agreement of ΔDIC_{TA-eq,3'→1} vs. pCO₂ and ΔDIC_{TA-eq,1'→3} vs. pCO₂ curves at high *p*₁ values also corroborates the flow measurements. If the *p*₁ were 0.4 mbar instead, the deacidification and acidification processes would have significantly different slopes so the amounts of CO₂ captured during deacidification and released during acidification would be different, as shown in **Fig. S 1 e**.

Here we plot the ideal cycles for varying $TA_{3'}$ and fixed $p_1 = 0.4$ mbar, $p_3 = 1$ bar and $\Delta TA_{3 \rightarrow 1} = 0.21$ M (**Fig. S 1**). The plots illustrate the effect of varying $TA_{3'}$ on $w_{\text{cycle,ideal}}$, $\Delta \text{DIC}_{\text{TA-eq}}$, and \bar{w}_{ideal} .

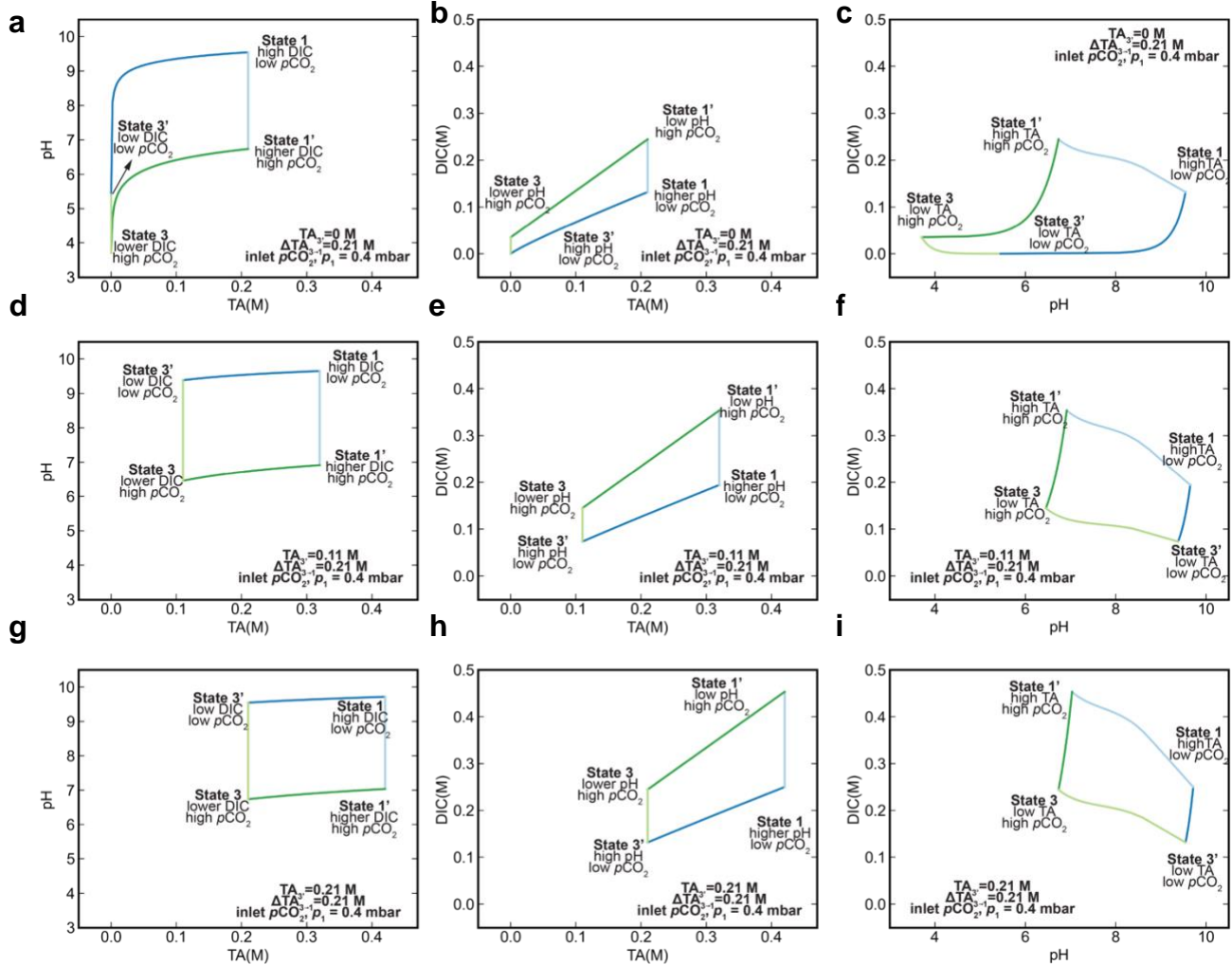


Fig. S 1 | Ideal cycles constructed using $p_1 = 0.4$ mbar and $p_3 = 1$ bar, $\Delta TA_{3 \rightarrow 1} = 0.21$ M and varying $TA_{3'}$. a-c, $TA_{3'} = 0.0$ M; d-f, $TA_{3'} = 0.11$ M and g-i, $TA_{3'} = 0.21$ M;

The area enclosed by the cycles in **Fig. S 1a, d** and **g**, is proportional to the ideal cycle work for the cycles with fixed $p_1 = 0.4$ mbar, $p_3 = 1$ bar, $\Delta TA_{3 \rightarrow 1} = 0.21$ M and $TA_{3'}$ being 0.0, 0.11 and 0.21 M, respectively. The area roughly stays the same as $TA_{3'}$ increases, but $\Delta \text{DIC}_{\text{TA-eq,3} \rightarrow 1}$ shrinks significantly, as shown in **Fig. S 1b, e** and **h**. As a result, \bar{w}_{ideal} increases as $TA_{3'}$ increases. With $TA_{3'}$ being 0.0, 0.11 and 0.21 M, the ideal cycle work is 3.58, 3.40 and 3.31 kJ L⁻¹, respectively, $\Delta \text{DIC}_{\text{TA-eq,3} \rightarrow 1}$ is 0.097, 0.049 and 0.005 M, respectively and the resulting \bar{w}_{ideal} is 37.02, 69.31 and 661.9 kJ molCO₂⁻¹, respectively.

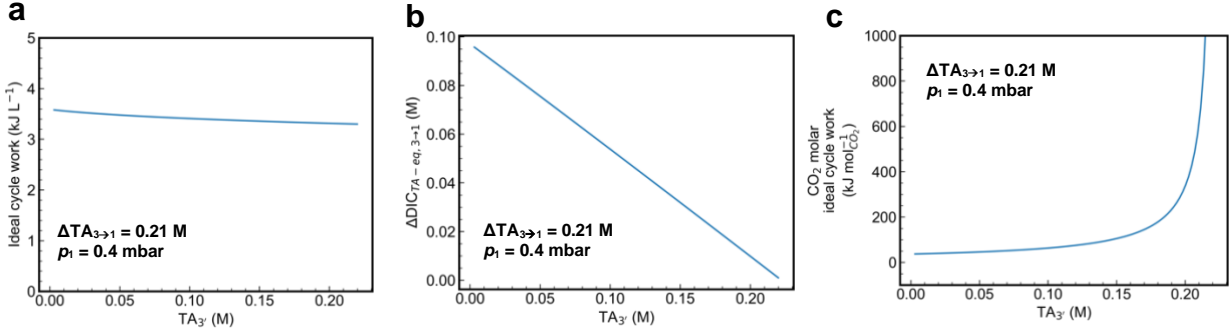


Fig. S 2| Dependence of (a) $w_{cycle,ideal}$, (b) $\Delta DIC_{TA-eq,3 \rightarrow 1}$ (c) and \bar{w}_{ideal} on $TA_{3'}$ in the ideal cycles with $p_1 = 0.4$ mbar, and $p_3 = 1$ bar, $\Delta TA_{3 \rightarrow 1} = 0.21$ M.

Fig. S 2 shows the dependence of $w_{cycle,ideal}$, $\Delta DIC_{TA-eq,3 \rightarrow 1}$ and \bar{w}_{ideal} on $TA_{3'}$. Again, \bar{w}_{ideal} increases with increasing $TA_{3'}$ because of the linearly decreasing $\Delta DIC_{TA-eq,3 \rightarrow 1}$ in the denominator of eq. S11.

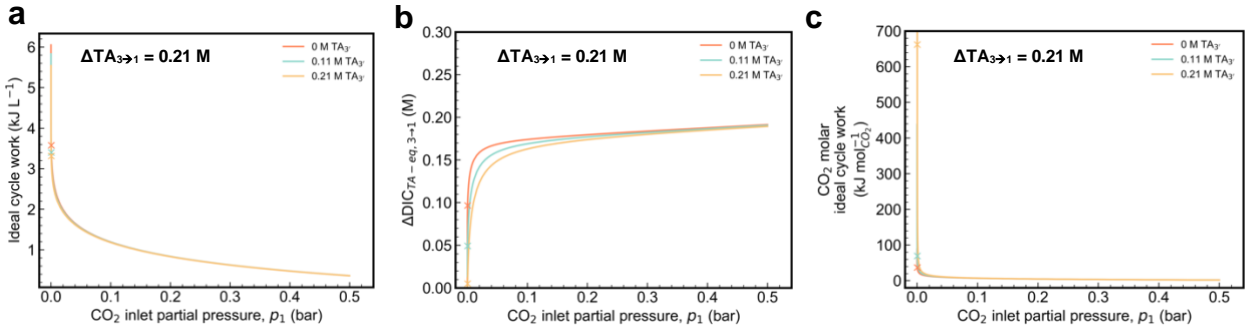


Fig. S 3| Dependence of (a) $w_{cycle,ideal}$, (b) $\Delta DIC_{TA-eq,3 \rightarrow 1}$ and (c) \bar{w}_{ideal} on p_1 in the ideal cycles with $\Delta TA_{3 \rightarrow 1} = 0.21$ M and $TA_{3'} = 0.0, 0.11$ and 0.21 M. The 'x' marks indicate $p_1 = 0.4$ mbar.

Fig. S 3 shows the dependence of $w_{cycle,ideal}$, $\Delta DIC_{TA-eq,3 \rightarrow 1}$ and \bar{w}_{ideal} on p_1 . $w_{cycle,ideal}$ decreases as p_1 increases because of lower negolyte pH, hence cell potential, during deacidification, but the curves are almost identical for different $TA_{3'}$ values. The $\Delta DIC_{TA-eq,3 \rightarrow 1}$ vs. p_1 curves for different $TA_{3'}$ are similar for large pCO_2 values, but significantly different at low p_1 . Therefore, to keep \bar{w}_{ideal} low for any inlet pressure p_1 , high $TA_{3'}$ should be avoided.

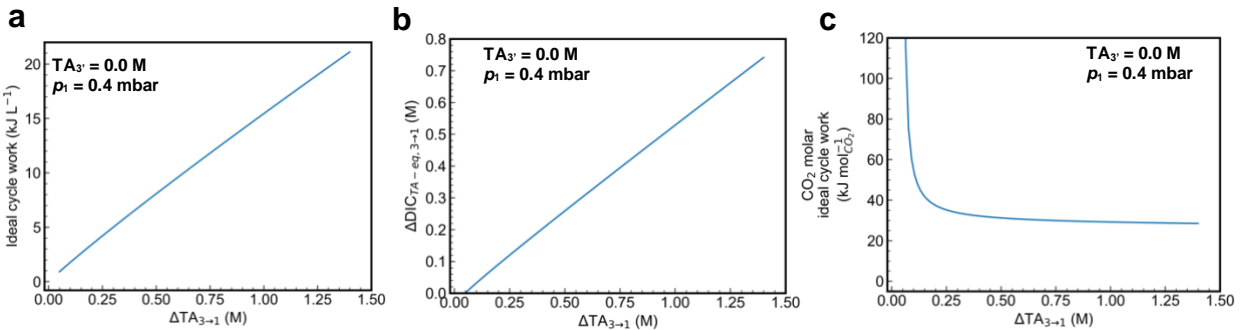


Fig. S 4| Dependence of (a) $w_{cycle,ideal}$, (b) $\Delta DIC_{TA-eq,3 \rightarrow 1}$ and (c) \bar{w}_{ideal} on $\Delta TA_{3 \rightarrow 1}$ in the ideal cycles with $p_1 = 0.4$ mbar, $p_3 = 1$ bar and $TA_{3'} = 0.0$ M.

The last parameter that affects $w_{cycle,ideal}$, $\Delta DIC_{TA-eq,3 \rightarrow 1}$ and \bar{w}_{ideal} is $\Delta TA_{3 \rightarrow 1}$, which is equivalent to twice the amount of DSPZ concentration. DSPZ has a solubility of 0.7 M in 1 M KCl or 1 M

KOH aqueous solution, so the largest $\Delta TA_{3 \rightarrow 1}$ it can induce is 1.4 M. **Fig. S 4** shows the dependence of $w_{\text{cycle,ideal}}$, $\Delta \text{DIC}_{\text{TA-eq},3 \rightarrow 1}$ and \bar{w}_{ideal} on $\Delta TA_{3 \rightarrow 1}$ for cycles with $TA_{3'} = 0.0$ M, $p_1 = 0.4$ mbar and $p_3 = 1$ bar. Not surprisingly, $w_{\text{cycle,ideal}}$ and $\Delta \text{DIC}_{\text{TA-eq},3 \rightarrow 1}$ increase with $\Delta TA_{3 \rightarrow 1}$ but the difference in their increase rate causes \bar{w}_{ideal} to decrease with larger $\Delta TA_{3 \rightarrow 1}$. At 1.4 M $\Delta TA_{3 \rightarrow 1}$, \bar{w}_{ideal} is 28.45 kJ mol_{CO₂}⁻¹, which is 23% lower than 37.02 kJ mol_{CO₂}⁻¹ for 0.21 M $\Delta TA_{3 \rightarrow 1}$. Assuming that similar second law efficiency holds for experimental cycles with different $\Delta TA_{3 \rightarrow 1}$ and same p_1 , p_3 and $TA_{3'}$, using higher concentration of DSPZ can further decrease the cycle work for CO₂ separation from 108.1 kJ mol_{CO₂}⁻¹ to 99.5 kJ mol_{CO₂}⁻¹. With the same reasoning, if a PCET molecule that undergoes 2-e⁻ transfer and has 10 M solubility is developed, the ideal cycle work could be as low as 24 kJ mol_{CO₂}⁻¹, leading to an actual cycle work of 95 kJ mol_{CO₂}⁻¹.

2 Cycle Data

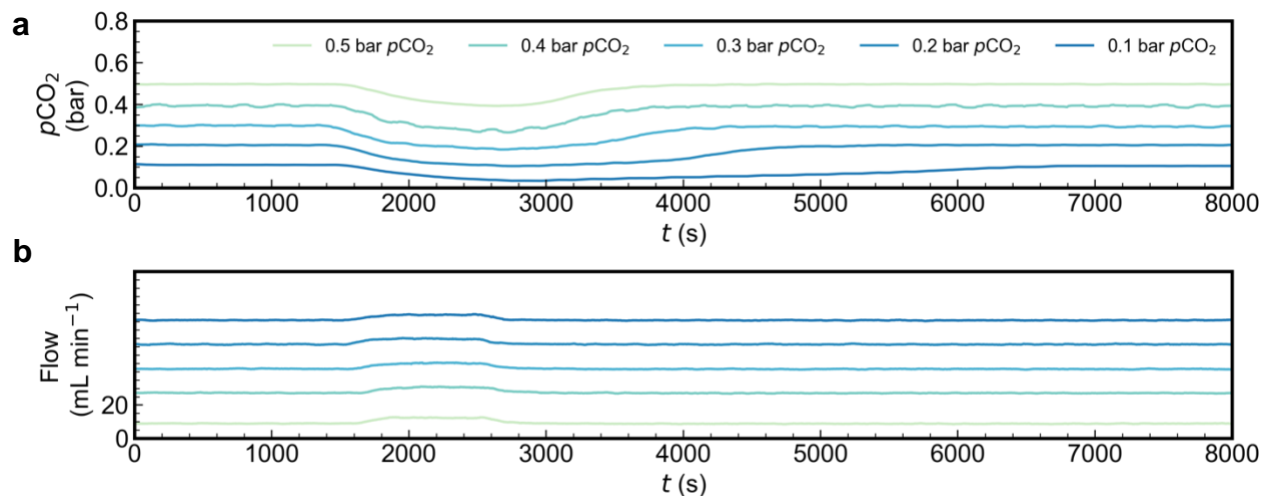


Fig. S 5| Duration of the CO₂ capture and release processes in the cycles with 40 mA cm⁻² current density. a, Downstream pCO₂ of one capture half cycle for each of the inlet pCO₂ conditions. **b,** Filtered total gas flow rate of one outgassing half cycle for each of the inlet pCO₂ conditions. All the processes look identical because of the same exit condition, so an arbitrary offset is added to differentiate the curves.

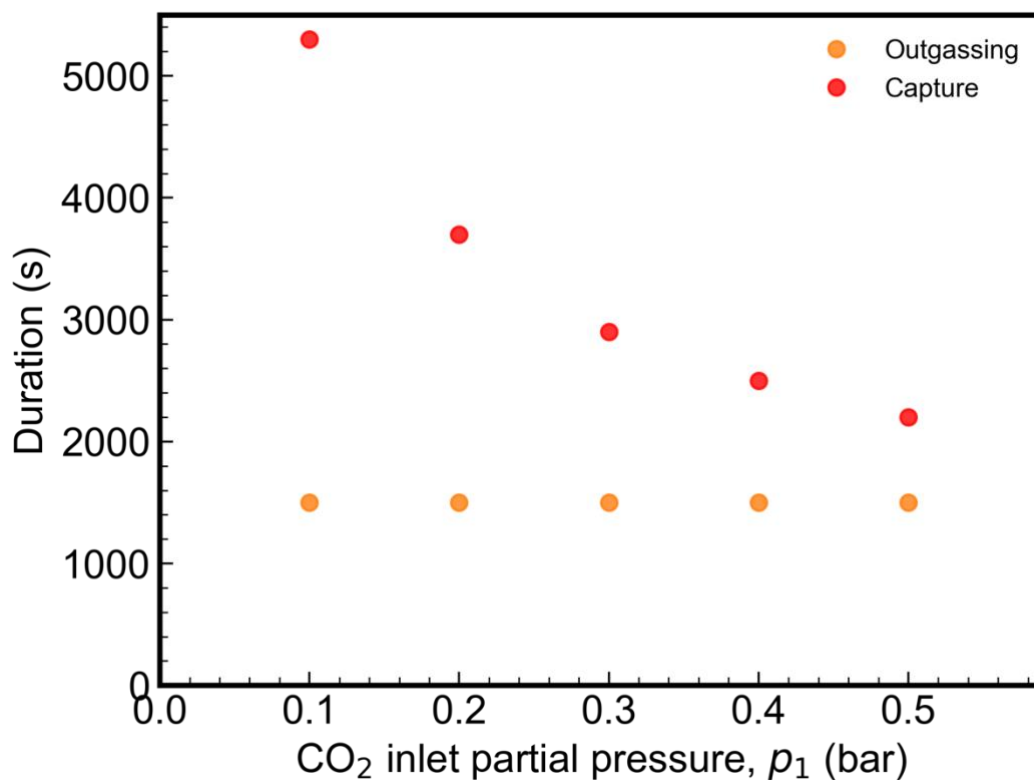


Fig. S 6| Capture and outgassing durations extracted from Fig. S 5 a and b.

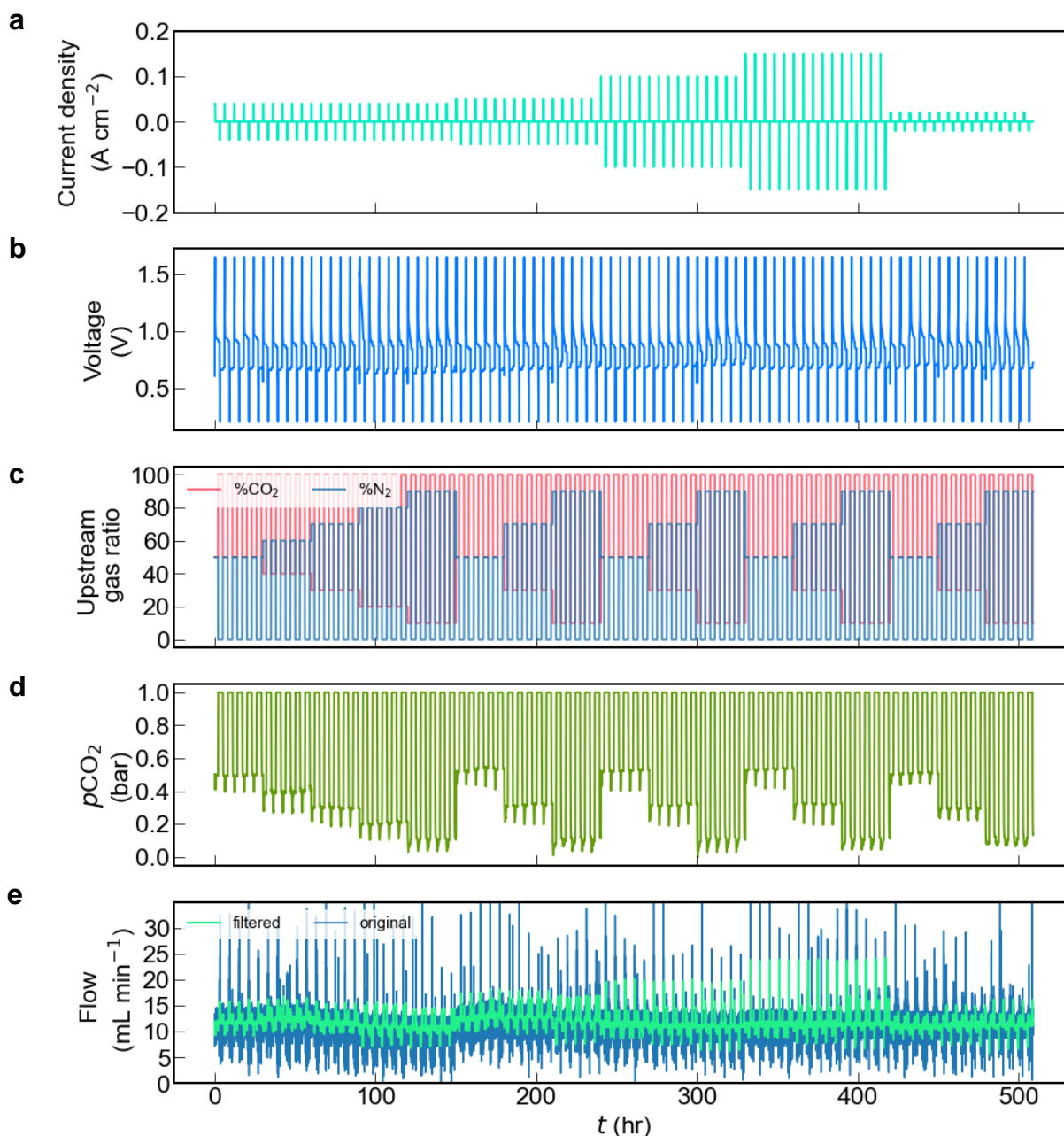


Fig. S 7| Eighty-five CO₂ concentrating cycles with varying inlet $p\text{CO}_2$ and current densities. These are the raw data for Fig. 5. Same cell was used as in **Fig 2**. Liquid pumping rate is 50 mL min⁻¹ for all the cycles. Note that, the pH measurements for high current densities are inaccurate, as the pH should never be able to reach pH > 14 for 0.11 M DSPZ. **a**, Current density. **b**, Voltage. **c**, N₂ and CO₂ percentage in the upstream source gas, controlled by mass flow controllers. **d**, CO₂ partial pressure. **e**, Total gas flow rate.

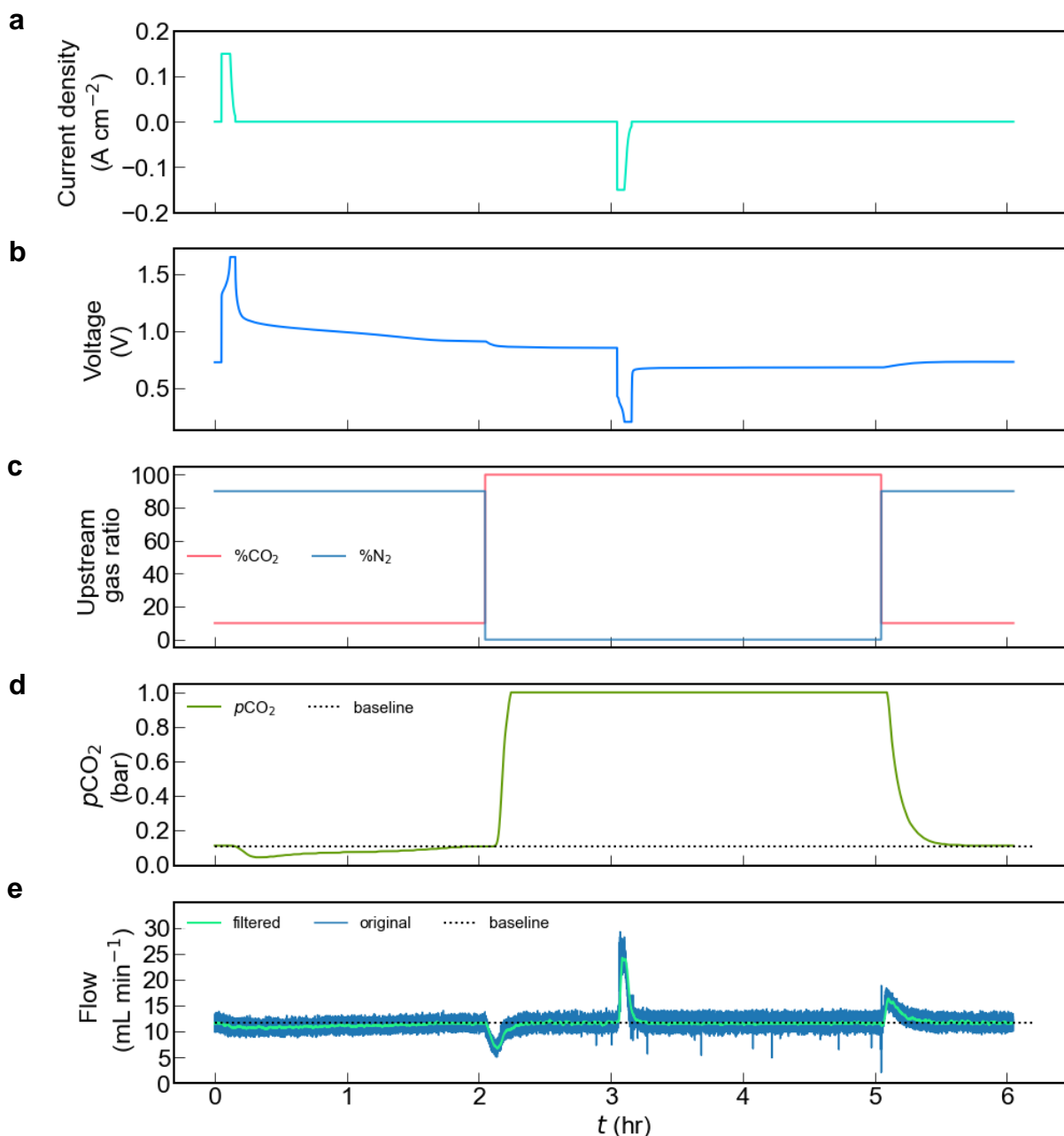


Fig. S 8| One CO_2 concentrating cycle from Fig. S 7 with 0.1 bar inlet $p\text{CO}_2$ and 1 bar exit $p\text{CO}_2$ at 150 mA cm^{-2} . Note that, the pH measurements are not shown because of an inexplicable artifact only present at high current, so it is invalid to extract $\text{DIC}_{\text{TA-pH}}$ for this condition. However, $\text{DIC}_{\text{TA-eq}}$ can be extracted because sufficient gas-solution is reached, as demonstrated by fact that the $p\text{CO}_2$ and flow curves return to their baselines after CO_2 invasion and outgassing. **a**, Voltage profile. **b**, Current density. **c**, N_2 and CO_2 percentage in the upstream source gas, controlled by MFC. **d**, CO_2 partial pressure. **e**, Total gas flow rate.

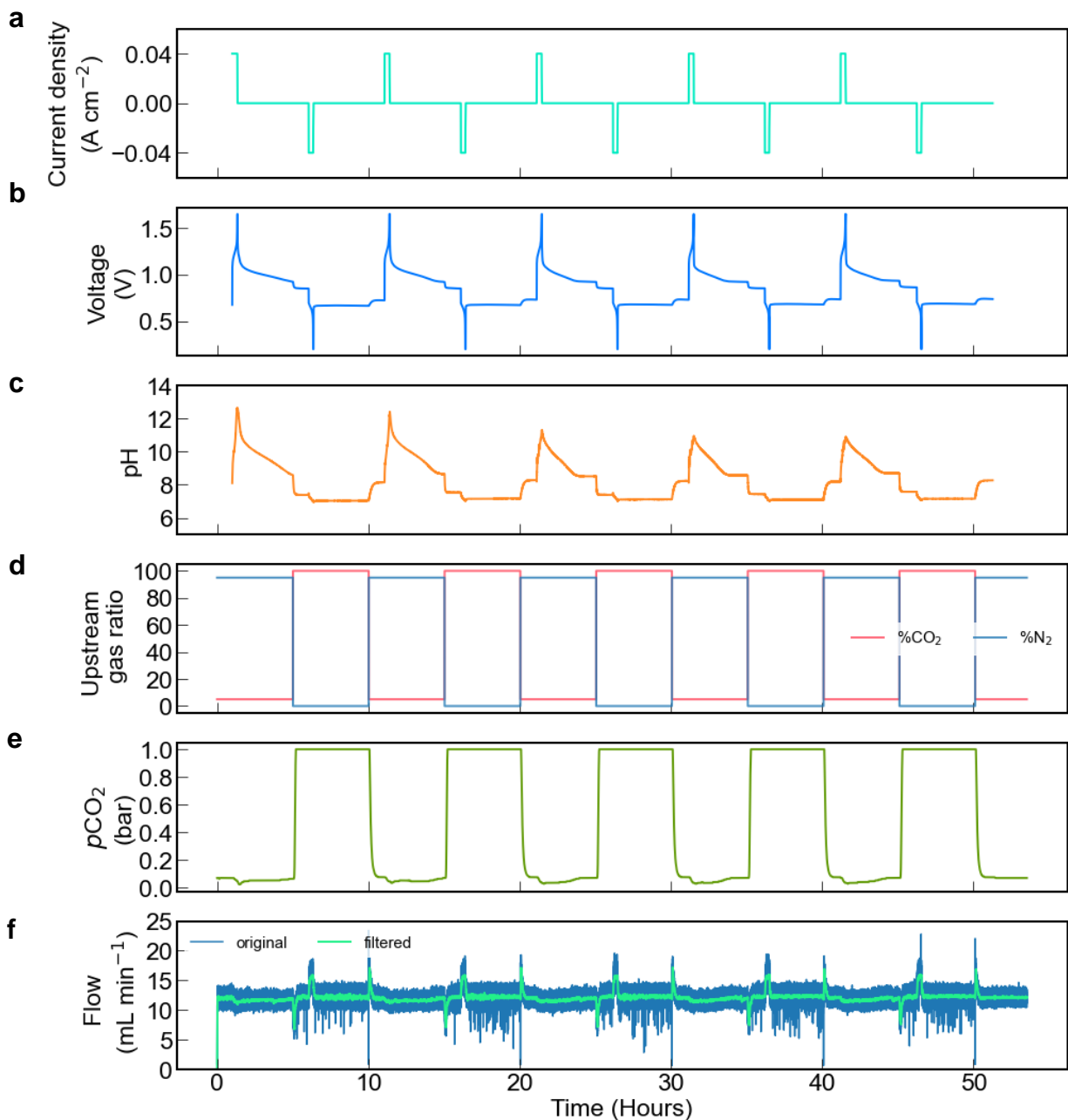
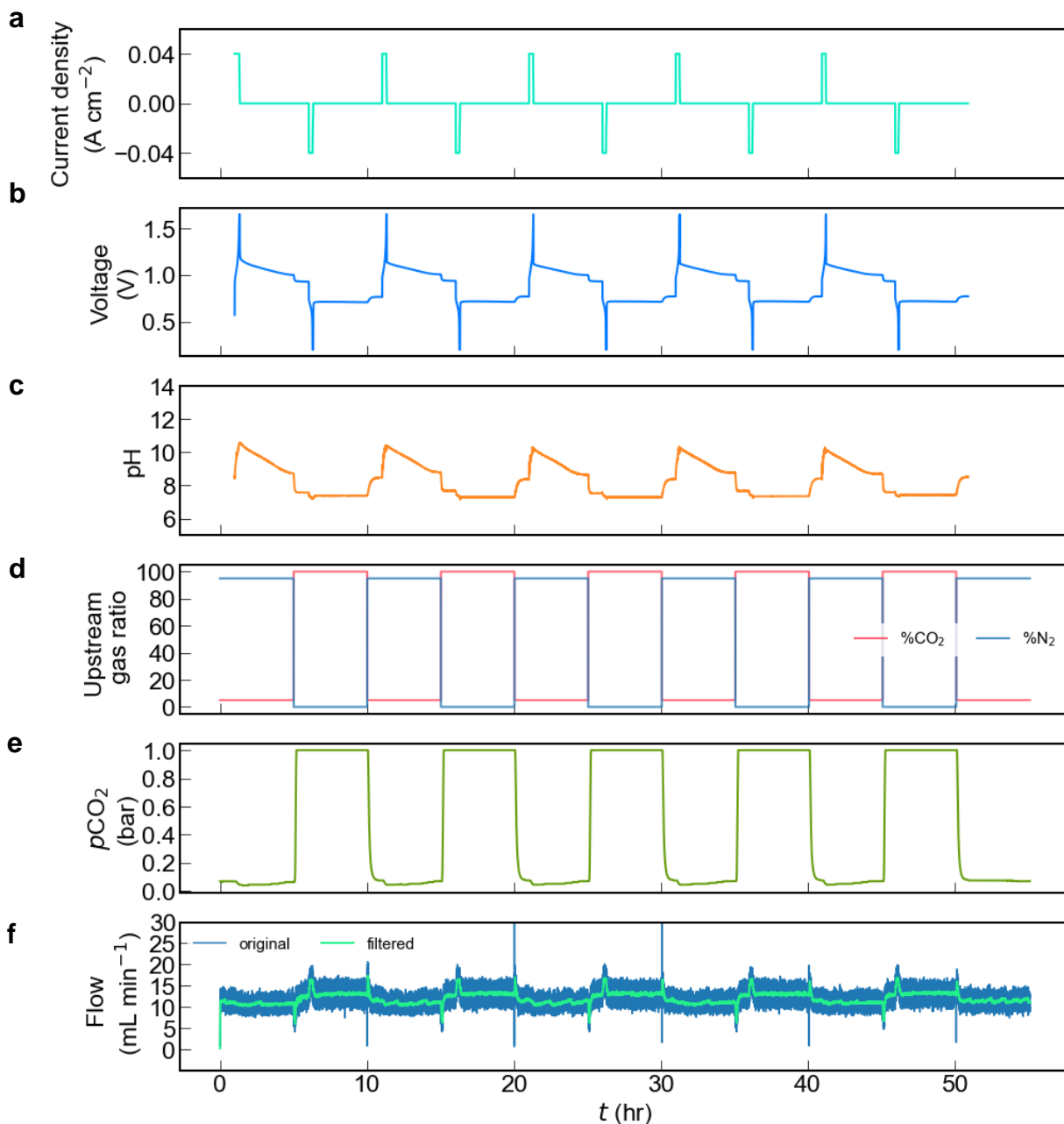


Fig. S 9| Five CO₂ concentrating cycles with 0.05 bar inlet $p\text{CO}_2$ and 1 bar exit $p\text{CO}_2$ at 40 mA cm⁻². Same cell was used as in Fig. 2. Fresh negolyte and posolyte were used. The liquid pumping rate is 150 mL min⁻¹, which is 50% faster than for capture at higher inlet pressure. **a**, Voltage profile. **b**, Current density. **c**, pH of the negolyte. **d**, N₂ and CO₂ percentage in the upstream source gas, controlled by mass flow controllers. **e**, CO₂ partial pressure. **f**, Total gas flow rate.

228
229



230
231
232
233
234
235
236

Fig. S 10| Post-electrochemical rebalancing CO_2 capture with 0.05 bar inlet $p\text{CO}_2$ and 1 bar exit $p\text{CO}_2$ at 40 mA cm^{-2} . Same cell was used as in Fig.2. Same posolyte and negolyte as in Fig. S 9 were used. The liquid pumping rate is 150 mL min^{-1} . **a**, Voltage profile. **b**, Current density. **c**, pH of the negolyte. **d**, N_2 and CO_2 percentage in the upstream source gas, controlled by mass flow controllers. **e**, CO_2 partial pressure. **f**, Total gas flow rate. The system has the same carbon capture/release capability after the post-electrochemical rebalancing.

3 More on Electrochemical Rebalancing

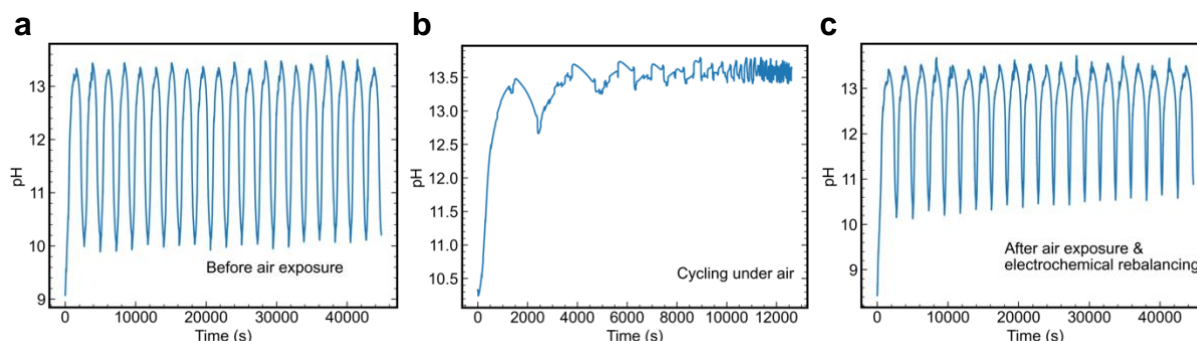


Fig. S 11| pH of the negolyte during cycles before air exposure (a), under air (b) and after electrochemical rebalancing (c), respectively. pH drifts up because of oxygen presence.

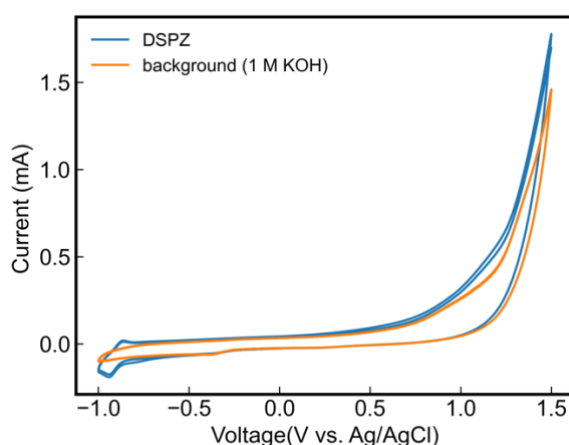


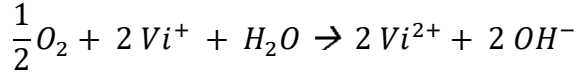
Fig. S 12| Cyclic voltammetry of DSPZ and 1 M KOH background. No additional peak was observed for DSPZ during the oxidative scan, indicating absence of side reactions.

Fig. 1b lists all the reactions related to carbon capture in our system. When all reactions involving CO_2 are removed, the system is the same as an aqueous organic redox flow battery (AORFB).³⁻⁵ The electrochemical rebalancing method is also applicable to AORFB when there is an oxygen leakage. **Fig. 6** demonstrates the application of the electrochemical rebalancing method in an AORFB and carbon capture flow cell, which both are organic PCET systems that have pH swing ranging from neutral to basic. Here we suggest that the electrochemical rebalancing method also applies to other aqueous based electrochemical systems, including organic and inorganic, PCET or non-PCET, acidic or basic, dissolved or solid redox active materials. If no side reaction is triggered by the oxidative voltage, which is the case for DSPZ as shown in **Fig. S 12**, the electrochemical rebalancing method can be applied. Here are several examples.

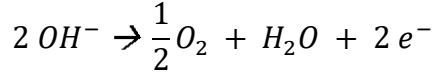
Organic Non-PCET system in neutral aqueous solution: $\text{Fe}(\text{CN})_6$ (posolyte) / Viologen (negolyte) Flow Battery

When the viologen-based redox flow battery⁶⁻⁸ is charged: oxygen can chemically oxidize the reduced viologen to the oxidized state, accumulating hydroxide in the negolyte, leading to the negolyte to discharged state and the posolyte active species maintaining the oxidized state. Because the redox active core of viologens have two positive charges, we denote their oxidized

form as Vi^{2+} and the single-electron reduced form as Vi^+ . The negolyte side is discharged when oxygen is present, i.e. :



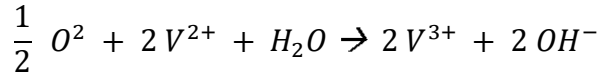
The electrochemical rebalancing method can remove the accumulated hydroxide, repelling O_2 in the negolyte reservoir:



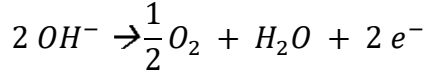
During the electrochemical rebalancing process, the electrons are transferred to the posolyte side, which has accumulated $\text{Fe}(\text{CN})_6^{3-}$, and eventually both negolyte and posolyte sides are recover the their initial composition, i.e. $\text{Fe}(\text{CN})_6^{4-}$ in posolyte and Vi^{2+} in negolyte, rebalancing the system.

Inorganic Non-PCET system in strongly acidic aqueous solution: $\text{VO}^{2+}/\text{VO}_2^+$ (posolyte) / $\text{V}^{3+}/\text{V}^{2+}$ (negolyte) Flow Battery

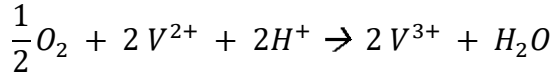
When a vanadium redox flow battery⁹ negolyte contains the charged form, i.e. V^{2+} : if oxygen diffuses into the negolyte, it can chemically oxidize V^{2+} to V^{3+} , and hydroxide is accumulated in the negolyte,



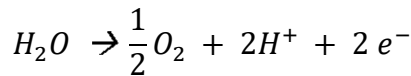
The electrochemical rebalancing method can remove the accumulated hydroxide, repelling O_2 :



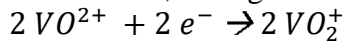
Because the electrolyte of a vanadium redox flow battery is strongly acidic, the hydroxide is readily neutralized and forming water. Hence the oxidation reaction is the following:



Therefore, instead of generating two hydroxides in the negolyte, the oxidation by oxygen reaction causes the loss of two protons. And the electrochemical rebalancing method in such scenario is as follows:



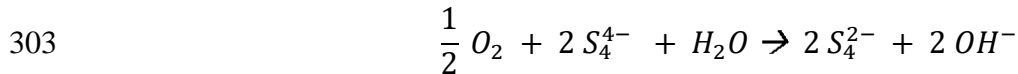
During the electrochemical rebalancing process, the electrons are transferred to the posolyte side, which has accumulated the oxidized form VO_2^+ , through



, and eventually both negolyte and posolyte sides are fully discharged (VO_2^+ in posolyte and V^{3+} in negolyte), thus rebalancing the system.

Inorganic Non-PCET system in basic aqueous solution: air (posolyte) / $\text{S}_4^{2-}/\text{S}_4^{4-}$ (negolyte) Battery

When a sulfur-air flow battery¹⁰ is charged: if oxygen diffuses into polysulfide negolyte, oxygen can chemically oxidize polysulfide, and hydroxide is accumulated in the negolyte,



304 The electrochemical rebalancing method can remove the accumulated hydroxide, repelling O₂:

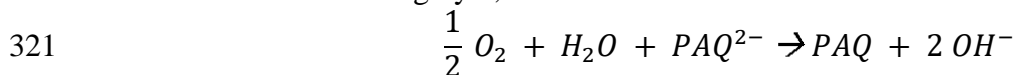


306 During the electrochemical rebalancing process, the electrons are transferred to the posolyte side
307 externally, thus rebalancing the system.

308
309 *Solid polyquinone Non-PCET system for carbon capture: LiFePO₄ (cathode) / Polyquinone*
310 *(anode)*

311
312 Liu et al.¹¹ demonstrated a solid quinone aqueous carbon capture system, where the cathode is
313 LiFePO₄ and the anode is polyquinone (PAQ) tethered to a carbon electrode. The authors utilized
314 a 20 molal LiTFSI aqueous solution to ensure that the reduced PAQ are deprotonated, i.e. PAQ²⁻,
315 which then binds with CO₂ to form PAQ-CO₂ adduct. Although the influence of oxygen in this
316 system is rather small, but side reaction still happens and can cause long term imbalance
317 (accumulation of oxidized cathode material and accumulated LiOH in the anode side).

318
319 When the anode is charged: oxygen can chemically oxidize the air-sensitive anode, and hydroxide
320 is accumulated in the negolyte,



322 The electrochemical rebalancing method can remove the accumulated hydroxide, repelling O₂:



324 During the electrochemical rebalancing process, the electrons are transferred to the cathode side
325 externally, eventually both anode and cathode are discharged, rebalancing the system.

326
327

References

1. Roy, R. N.; Roy, L. N.; Vogel, K. M.; Portermore, C.; Pearson, T.; Good, C. E.; Millero, F. J.; Campbell, D. M., The Dissociation Constants of Carbonic Acid in Seawater at Salinities 5 to 45 and Temperatures 0 to 45 °C. *Mar Chem* **1993**, *44* (2-4), 249-267.
2. Jin, S.; Wu, M.; Gordon, R. G.; Aziz, M. J.; Kwabi, D. G., pH swing cycle for CO₂ capture electrochemically driven through proton-coupled electron transfer. *Energy & Environmental Science* **2020**, *13* (10), 3706-3722.
3. Hollas, A.; Wei, X. L.; Murugesan, V.; Nie, Z. M.; Li, B.; Reed, D.; Liu, J.; Sprengle, V.; Wang, W., A biomimetic high-capacity phenazine-based anolyte for aqueous organic redox flow batteries. *Nat Energy* **2018**, *3* (6), 508-514.
4. Jin, S.; Jing, Y.; Kwabi, D. G.; Ji, Y.; Tong, L.; De Porcellinis, D.; Goulet, M. A.; Pollack, D. A.; Gordon, R. G.; Aziz, M. J., A water-miscible quinone flow battery with high volumetric capacity and energy density. *ACS Energy Letters* **2019**, *4* (6), 1342-1348.
5. Ji, Y.; Goulet, M. A.; Pollack, D. A.; Kwabi, D. G.; Jin, S.; Porcellinis, D.; Kerr, E. F.; Gordon, R. G.; Aziz, M. J., A phosphonate-functionalized quinone redox flow battery at near-neutral pH with record capacity retention rate. *Advanced Energy Materials* **2019**, *9* (12), 1900039.
6. Beh, E. S.; De Porcellinis, D.; Gracia, R. L.; Xia, K. T.; Gordon, R. G.; Aziz, M. J., A Neutral pH Aqueous Organic-Organometallic Redox Flow Battery with Extremely High Capacity Retention. *ACS Energy Letters* **2017**, *2* (3), 639-644.
7. Jin, S.; Fell, E. M.; Vina-Lopez, L.; Jing, Y.; Michalak, P. W.; Gordon, R. G.; Aziz, M. J., Near Neutral pH Redox Flow Battery with Low Permeability and Long-Lifetime Phosphonated Viologen Active Species. *Advanced Energy Materials* **2020**, *10* (20), 2000100.
8. Luo, J.; Hu, B.; Debruler, C.; Bi, Y. J.; Zhao, Y.; Yuan, B.; Hu, M. W.; Wu, W. D.; Liu, T. L., Unprecedented Capacity and Stability of Ammonium Ferrocyanide Catholyte in pH Neutral Aqueous Redox Flow Batteries. *Joule* **2019**, *3* (1), 149-163.
9. Mena, E.; Lopez-Vizcaino, R.; Millan, M.; Canizares, P.; Lobato, J.; Rodrigo, M. A., Vanadium redox flow batteries for the storage of electricity produced in wind turbines. *International Journal of Energy Research* **2018**, *42* (2), 720-730.
10. Li, Z.; Pan, M. S.; Su, L.; Tsai, P. C.; Badel, A. F.; Valle, J. M.; Eiler, S. L.; Xiang, K.; Brushett, F. R.; Chiang, Y. M., Air-Breathing Aqueous Sulfur Flow Battery for Ultralow-Cost Long-Duration Electrical Storage. *Joule* **2017**, *1* (2), 306-327.
11. Liu, Y.; Ye, H.-Z.; Diederichsen, K. M.; Voorhis, T. V.; Hatton, T. A., Electrochemically mediated carbon dioxide separation with quinone chemistry in salt-concentrated aqueous media. *Nature Communications* **2020**, *11*, 2278.